

# **Dynamic simulation of a novel nuclear hybrid energy system with large-scale hydrogen storage in an underground salt cavern**

**<sup>1</sup>An Ho, <sup>1</sup>Kasra Mohammadi, <sup>2</sup>Matthew Memmott, <sup>2</sup>John Hedengren, <sup>1,3</sup>Kody M. Powell**

<sup>1</sup>University of Utah, Department of Chemical Engineering, 50 South Central Campus Dr., 3290  
MEB, Salt Lake City, UT 84112-9203, USA

<sup>2</sup>Brigham Young University, Department of Chemical Engineering, Engineering Building,  
Provo, UT 84602, USA

<sup>3</sup>University of Utah, Department of Mechanical Engineering, 1495 E 100 S, Salt Lake City, UT  
84112, USA

## **Abstract**

In this study, a nuclear hybrid energy system (NHES) with large-scale hydrogen storage integrated with a gas turbine cycle is proposed as a flexible system for load following. The proposed system consists of a nuclear reactor, a steam Rankine cycle, a hydrogen electrolyzer, a storage system for hydrogen in an underground salt cavern, and a Brayton cycle that uses hydrogen as fuel to generate additional electricity to meet peak demand. A dynamic mathematical model is developed for each subsystem of the NHES. To evaluate the potential benefits of the system, a one-year study is conducted, using scaled grid demand data from ISO New England. The dynamic simulation results show that the system is capable of meeting the demand of the grid without additional electricity from outside sources for 93% of the year, while decreasing the number of ramping cycles of the nuclear reactor by 92.7%. There is also potential for economic benefits as the system only had to ramp up and down 7.4% of the year, which increased the nuclear capacity factor from 86.3% to 98.3%. The simulation results show that the proposed hybrid system

improves the flexibility of nuclear power plants, provides more electricity, and reduces greenhouse gas emissions.

**Keywords:** Nuclear Hybrid Energy Systems; Flexible Load Following; Renewable Energy; Large Scale Hydrogen Storage; Hydrogen Gas Turbine.

## Nomenclature

### Abbreviations

|      |                               |
|------|-------------------------------|
| LCOE | Levelized cost of electricity |
| LWR  | Light Water Reactor           |
| NHES | Nuclear Hybrid Energy System  |
| PEM  | Polymer Electrolyte Membrane  |
| SMR  | Small Modular Reactor         |

### Symbols

|                  |                                          |
|------------------|------------------------------------------|
| $n_{neu}$        | Neutron density                          |
| $t$              | Time                                     |
| $T$              | Temperature                              |
| $V$              | Volume                                   |
| $C_p$            | Heat capacity                            |
| $W$              | Power                                    |
| $\dot{m}$        | Mass flow rate                           |
| $E_f$            | Average recoverable energy per fission   |
| $\sigma_f^{235}$ | Microscopic cross section of Uranium 235 |
| $N_{235}$        | Atomic number density of Uranium 235     |
| $\eta$           | Efficiency                               |
| $P$              | Pressure                                 |
| $I$              | Current                                  |
| $R$              | Gas constant                             |
| $Vol$            | Real cell voltage                        |
| $n$              | Number of moles                          |
| $z_{comp}$       | Hydrogen compressibility factor          |
| $\dot{N}$        | Molar flow rate                          |

### Subscripts

|         |                      |
|---------|----------------------|
| $in$    | Inlet                |
| $out$   | Outlet               |
| $turb$  | Turbine              |
| $therm$ | Thermal              |
| $core$  | Nuclear reactor core |

|           |                          |
|-----------|--------------------------|
| $H_2$     | Hydrogen                 |
| $w$       | Wall                     |
| $cav$     | Cavern                   |
| $comp$    | Compressor               |
| $elec$    | Electrolyzer             |
| $nom$     | nominal                  |
| $a$       | Air                      |
| $e$       | Exhaust                  |
| $amb$     | Ambient                  |
| $GasTurb$ | Gas turbine              |
| $Brayton$ | Brayton cycle            |
| $ideal$   | Ideal                    |
| $actual$  | Actual                   |
| $f$       | Fuel                     |
| $fire$    | Turbine firing condition |

## 1. Introduction

The electricity market in the United States is moving away from fossil fuel sources and towards a mixed energy source market, with emphasis on renewable energy such as solar, wind, etc. However, an increase in variable renewable energy sources in the grid system causes technical and economic challenges due to the high variability, intermittency and low-capacity factors of renewable energy plants [1], [2], [3]. Power systems with integrated renewable energy sources require greater system flexibility at all times to make sure the supply-demand balance is maintained [4], [5], [6]. To meet the demands that are not met by renewable energy sources, load following power plants are usually needed to replace the renewable sources during peak demands. Natural gas power plants are usually used for this purpose [7], which have low capital cost and high operating cost and emit significant greenhouse gases [8]. To be able to decarbonize and work towards a green and clean future of electricity, traditional and reliable sources must be replaced by other low or free carbon sources such as nuclear power plants [9], [10].

Nuclear power plants offer several benefits such as high reliability, high-capacity factors, and a low carbon footprint [11]. However, to maximize the benefit of nuclear power plants, they

must be operated at maximum capacity at all times to minimize the levelized cost of electricity (LCOE) for these plants. Further, accelerated fuel depletion can develop when nuclear power plants have to ramp up and down to meet the grid demand. Nuclear power plants often operate at “base load” during low demand time, and sell surplus electricity to the grid usually at low or negative prices [8], [12]. This is because renewable energies peak at certain times of the day, which leads to volatile daily prices. During high renewable capacities, the market price of electricity can go down to negative values [13].

Nuclear power’s problem of inflexibility is due to both technical and economic reasons. Nuclear reactors adjust power primarily by changing the control rods positions to moderate the power output. Changing the position of the control rods drastically changes the neutron flux profile surrounding the fuel assemblies, which in turn changes the heating rate around the control rods. This power change causes the fuel assembly temperature to undergo immediate and significant changes. Fuel pellets and cladding undergo serious thermal and mechanical stresses that can result in the fuel pellets cracking or the cladding failing [12], [14], [15]. Hence, the speed at which the control rods can be inserted or withdrawn is controlled by the Nuclear Regulatory Commission [12]. As a result, nuclear power can be difficult to integrate into an increasingly diverse electricity market, with more and more carbon-free renewable sources.

However, studies have shown that integrating nuclear power plants with other sources can increase the flexibility and reliability of the system, reduce the cost, maximize revenues, and help meet greenhouse gas reduction goals [12]. These integrated hybrid energy systems store and/or use the excess electricity/heat to produce different commodities [16], [17], [18]. This will allow the base load operation of nuclear power plants and other renewable sources to minimize cost,

maximize profit and provide low-carbon electricity generation to the grid. An example of such a nuclear generated commodity is hydrogen.

Hydrogen is a promising fuel that is light, storable, and most importantly, does not produce any pollutants or greenhouse gases. It is the most energy dense of any known fuel material [19]. It is also a very valuable commodity, with its demand rising more than 300% since 1975, and it is expected to continue to rise in the next decades [20]. Hydrogen is used in different industries including oil refining, methanol production, ammonia synthesis, etc. It can also be used in transportation, building heating (especially for multifamily or commercial buildings), and power generation [21]. Hydrogen has been used for storing renewable energy, as well as in gas turbines to produce electricity. The International Energy Agency (2019) emphasized the potential of hydrogen to facilitate the transition into a cleaner, greener and more affordable energy future [21].

Salt caverns have been used to store various forms of energy including oil, natural gas, and hydrogen [22]. Salt cavern storage is considered among the most promising underground gas storage options due to the large sealing capacity of rock salt, the low cushion gas requirement, the inert nature of salt caverns, and the ability to operate flexibly with high injection/withdrawal rates [23]. Currently, there are a few sites that store hydrogen in salt caverns such as Teeside, United Kingdom, and Clemens Dome, Spindletop and Moss Bluff in the United States [24]. Clemens Dome salt cavern facility has been in operation since 1983, and has shown remarkable resiliency and reliability, demonstrating that underground salt cavern hydrogen storage is a technically feasible option. Salt caverns also offer an economic incentive, as it can be up to 10 times less expensive than above ground storage tanks, as well as 20 times less than hard rock mines [25].

Numerous studies have been presented in the literature regarding different nuclear hybrid energy systems. For example, Wang et al. [26] proposed a nuclear-solar hybrid system for

combined power and freshwater production. The authors proposed a novel design of a nuclear-solar hybrid power plant with heavy liquid metal as the heat transfer medium. A technical and economic analysis was performed to evaluate the performance of the hybrid model. The results showed that the proposed design was technically feasible, and had an annual cost saving of \$680,423 compared with a desalination system powered by a coal-fired plant. Ingersoll et al. [27] proposed a desalination system powered by a small modular nuclear reactor. In the proposed hybrid system, the nuclear plant, a NuScale module, was combined with three different desalinations systems: multi-effect distillation, multi-stage flash distillation, and reverse osmosis. The results showed that the nuclear power plant could be effectively coupled with a water desalination plant. Epiney et al. [6] carried out an economic analysis of a hybrid nuclear system in a grid system with wind turbines. The authors used a new methodology to evaluate the economic performance of the hybrid system. The new methodology incorporates the stochastic characteristics of a nuclear-renewable hybrid energy system like wind speed or electricity demands. The results showed that under the right conditions, with suitable industrial processes being added, the hybrid system could provide economic benefits. Zhao et al. [28] proposed a novel design and performed a preliminary performance analysis on a hybrid nuclear-solar system using a molten-salt packed-bed thermal energy storage. The proposed system integrated a molten-salt concentrating solar power tower plant with small modular reactors. A thermal energy storage system was used to store and dispatch thermal energy whenever it is required. The proposed system was able to satisfy the power demand in a 7-day operation without the need for any heat generation restrictions. The results showed the technical feasibility of the hybrid system as well as the potential for a non-carbon emitting power generation system for load following applications.

A review of the literature also shows that there are a few studies on the dynamic modeling of hybrid nuclear hydrogen energy systems. Many reports and reviews have been presented about different technologies for hydrogen production with nuclear reactors [1], [29], [30]. Pinsky et al. [1] reviewed the current hydrogen generation technologies coupled with nuclear energy. It was shown that electrolysis and thermochemical water splitting technologies can easily be coupled with nuclear plants. El-Emam et al. [29] showed that with the current hydrogen generation technologies, nuclear energy is one of the main alternatives that can meet the required thermal/electrical needs for large-scale hydrogen production. Şahin et al. [30] specifically looked at coupling Gen IV nuclear reactors with hydrogen generation technologies. The authors discussed that nuclear energy can be used as the primary energy source for large-scale hydrogen production to achieve a sustainable energy future. Obrien et al. [31] carried out an analysis to evaluate large-scale hydrogen production using nuclear energy. However, in all of these studies, a steady-state analysis was conducted and flexible operation of nuclear power plants was not considered. Kim et al. [8] conducted a study on the dynamic performance of a high temperature steam electrolysis integrated with a nuclear hybrid energy system. However, the limitation of this study was that the dynamic simulation was limited to a 7-day period at the longest.

In this study, a novel nuclear-hydrogen hybrid system is proposed that integrates a small modular reactor (SMR) module with a steam Rankine cycle, a polymer electrolyte membrane (PEM) electrolyzer, a large-scale hydrogen storage system with an underground salt cavern, and a hydrogen gas turbine cycle. The primary objective of the study is to demonstrate the technical feasibility as well as the benefits of the proposed system under a highly variable grid demand requiring flexible outputs. A dynamic model is developed for each subsystem of the proposed hybrid system to simulate its performance for a year-long period, using real data from the grid. A

reliable control scheme is developed for the nuclear reactor and the hydrogen gas turbine. Using the developed dynamic model and control schemes, the technical feasibility of the proposed hybrid system is evaluated and then compared with a stand-alone nuclear power plant. The main novelty of this study is the proposal of a novel nuclear hybrid energy system and dynamic simulation of its performance for a period of one year.

The rest of the paper is organized as follows: Section 2 provides an overview of the nuclear hybrid system; Section 3 provides the detailed mathematical model formulation used to simulate each components of the system. Section 4 talks about the results of the dynamic simulation and the one-year period case study. Finally, Section 5 summarizes the main conclusions of the work.

## **2. Proposed System Overview**

This section briefly describes the proposed nuclear hybrid energy system with hydrogen generation and a hydrogen gas turbine. The nuclear hybrid energy system proposed in this study is shown schematically in Figure 1. The proposed system is divided into five different subsystems: (1) NuScale small modular reactor (SMR) module, (2) a steam Rankine power cycle, (3) an underground hydrogen storage, (4) a polymer electrolyte membrane (PEM) electrolyzer, and (5) a hydrogen gas turbine.





secondary loop. As it cools, the coolant is circulated downward until it reaches the core again. The loop is repeated as the coolant is heated up at the core and rises again. This flow is entirely maintained by natural buoyancy forces.

Superheated steam is generated in the secondary loop through the helical coil steam generator. Feed water is pumped into the tubes, where it is heated by the primary loop as it goes up through the steam generator, and comes out as superheated steam. The superheated steam is then distributed to the steam Rankine power cycle to produce electricity. The nominal capacity of the steam Rankine cycle is 49.95 MWe. Low-pressure steam exiting the turbine is condensed in a condenser and pumped back into the steam generator. The electricity produced by the Rankine cycle is distributed to the electrical grid to meet the demand from the grid, and also the demand of the energy storage element, which includes the energy required to drive the hydrogen electrolyzer and the hydrogen compressors.

The energy storage element consists of a hydrogen electrolyzer facility, a multi-stage compressor, and a salt cavern. When the electrical demand is low, the extra energy is used to generate hydrogen through the hydrogen electrolyzer, which is then compressed and pumped into the salt cavern for storage. The hydrogen electrolyzer facility is a large scale, central facility that uses electricity from the steam Rankine cycle to split water into hydrogen and oxygen. In this study, a PEM electrolyzer is used due to its advantages compared to other alkaline electrolysis systems [33]. A multi-staged compressor system, including five compressors, is used to compress the hydrogen into the salt cavern. The first stage compresses the hydrogen from the atmospheric pressure to 2 MPa. Then the next 4 stages of the compressors compress the hydrogen from 2 MPa to 17 MPa, which is the maximum pressure of the salt cavern. For the purpose of this paper, the

electrical requirement of the energy storage system consists of the electricity needed to split the water and produce hydrogen, and compress the hydrogen into the underground salt cavern.

The hydrogen generated and stored in the electrolyzer and salt cavern is used to generate additional electricity using a recuperative hydrogen gas turbine cycle. There is currently no commercially pure hydrogen gas turbine in operation. However, there are many companies working towards 100% hydrogen thermal gas turbines, such as such as Mitsubishi, Siemens, General Electrics, etc. as well as electricity companies preparing to transition to 100% hydrogen fuel in the next decade [34]. When the grid demand is higher than the nominal capacity of the steam turbine, the hydrogen is taken out of the salt cavern, decompressed to compressor outlet pressure, and burned in the gas turbine to supply additional electricity to the electrical grid.

### **3. Theoretical model**

A theoretical model based on the first law of thermodynamics, as well as mass and energy balances were developed for each components of the Nuclear Hybrid Energy system. The developed model was implemented and simulated in Matlab/Simulink [35].

#### **3.1 The Nuclear Reactor Model**

The dynamic model for the nuclear reactor is adopted from [36] and [37]. The following assumptions are made for the modeling of the nuclear reactor [36]:

- The dynamic model of the reactor is based on the point kinetics equations
- The reactor is assumed to be spatially homogenous
- A single group of delayed neutrons is assumed
- The elements of the reactor consist of the fuel, the moderator, and the control rods
- The effect of control rods position on reactivity is assumed to be quadratic [36]
- The mass flow rate of the coolant is assumed to be constant [38]

- The reactivity dependence on the fuel and moderator temperature are assumed to be linear
- The heat loss of the reactor is assumed to be negligible

The input of the model is the control rods position, measured in meters. The length is correlated to the model that is used, so that it can be used to access the impact on the neutronics more clearly. The output of the model is the thermal power of the nuclear reactor (MWth) as well as the temperature of the moderator and the fuel. The detailed mathematical equations for the neutron dynamics, thermodynamics of the nuclear reactor, the steam generator, and the steam Rankine cycle are presented in the Supplementary Materials. The thermal power of the nuclear core can be calculated as:

$$W_{therm} = n_{neu}(t) \sigma_f^{235} E_f N_{235} V_{core} \quad (1)$$

where  $n_{neu}(t)$  is the neutron density,  $E_f$  is the average recoverable energy per fission,  $\sigma_f^{235}$  is the microscopic cross section of Uranium 235,  $N_{235}$  is the atomic number density of Uranium 235 in the fuel,  $V_{core}$  is the total volume of the core.

### 3.2 Hydrogen Generation Model

Hydrogen is generated by using extra energy during low demand time by using a PEM water electrolyzer process. An electrochemical model of the electrolyzer is developed to calculate the amount of hydrogen produced as a function of power. The electrolyzer has four subsystems of the anode, the cathode, the membrane, and the voltage. The developed model for the PEM electrolyzer is adapted from [42] and [43]. The detailed description of the model used for the anode, cathode, membrane and the voltage subsystems are presented in the Supplementary Materials.

The efficiency of the electrolyzer is calculated as follows:

$$\eta_{elec} = \frac{P_{ideal}}{P_{actual}} \times 100\% \quad (2)$$

From [49], the ideal amount of power to generate 1 kg of hydrogen is 39 kWh. The actual amount of power can be calculated by Eq. (3):

$$P_{actual} = I V \quad (3)$$

where  $I$  is the current and  $V$  is the voltage.

### 3.3 Salt Cavern Model

The salt cavern model is composed of the material balance and energy balance inside the cavern, as presented by Eqs. (4) and (5):

$$\frac{dn_{H_2}}{dt} = \dot{N}_{H_2,in} - \dot{N}_{H_2,out} \quad (4)$$

$$n_{H_2} \frac{dT_{cav}}{dt} = \frac{\dot{N}_{H_2,in} C_{p,in} T_{in} + h_{cav}(T_w - T_{cav}) - \dot{N}_{H_2,out} C_{p,out} T_{out}}{C_{p,H_2} - T_{cav} \frac{dn_{H_2}}{dt}} \quad (5)$$

where  $h_{cav}$  is the convective heat transfer coefficient between the hydrogen gas inside the cavern and the wall of the cavern.  $T_w$  is the temperature of the wall, and  $T$  is the temperature of the hydrogen gas inside the cavern. The convective heat transfer coefficient is calculated using the correlation used by [50].

The pressure of the cavern can be calculated at each time step with:

$$P_{cav} = \frac{z_{comp} n_{H_2} R T_{cav}}{V_{cav}} \quad (6)$$

where  $z_{comp}$  is the compressibility factor of hydrogen, which can be calculated at each time step with the following correlation [51]:

$$z(P, T) = 1 + \sum_{i=1}^9 a_i \left( \frac{100K}{T} \right)^{b_i} \left( \frac{P}{1MPa} \right)^{c_i} \quad (7)$$

where  $a_i$ ,  $b_i$ , and  $c_i$  are constant coefficients, which can be found in [51].

The model for the hydrogen compressor and the minimum and maximum threshold of the salt cavern is presented in the Supplementary Materials.

### 3.4 Brayton Cycle Model

During peak demand times, hydrogen can be taken out of the cavern and burned in a gas turbine to produce electricity for the grid. The gas turbine model comprises of a compressor, combustion chamber, turbine, generator, and recuperator. The thermodynamics model is adapted from [8] and [54].

The detailed model of the compressor, the combustion chamber, the turbine, and the recuperator are presented in the Supplementary Materials. The overall power output of the plant can be calculated as:

$$W_{GasTurb} = (\dot{m}_f + \dot{m}_a)C_{p,e}(T_{fire} - T_e) - \dot{m}_a C_{p,a}(T_{comp,out} - T_{amb}) \quad (76)$$

where  $C_{p,a}$  is the heat capacity of air, which is assumed to be constant for this model,  $C_{p,e}$  is the exhaust gas heat capacity,  $\dot{m}_f$  is the fuel (hydrogen) flow rate,  $\dot{m}_a$  is the air flow rate,  $T_{fire}$  is turbine firing temperature,  $T_e$  is the turbine exhaust temperature,  $T_{comp,out}$  is the outlet temperature of the compressor.

The efficiency of the Brayton cycle can be calculated as follows:

$$\eta_{Brayton} = \frac{W_{GasTurb}}{\dot{m}_f LHV} \times 100\% \quad (79)$$

where LHV is lower heating value of the fuel.

### 3.5 System Controls

A detailed control scheme of the proposed NHES is shown schematically in Figure 2.

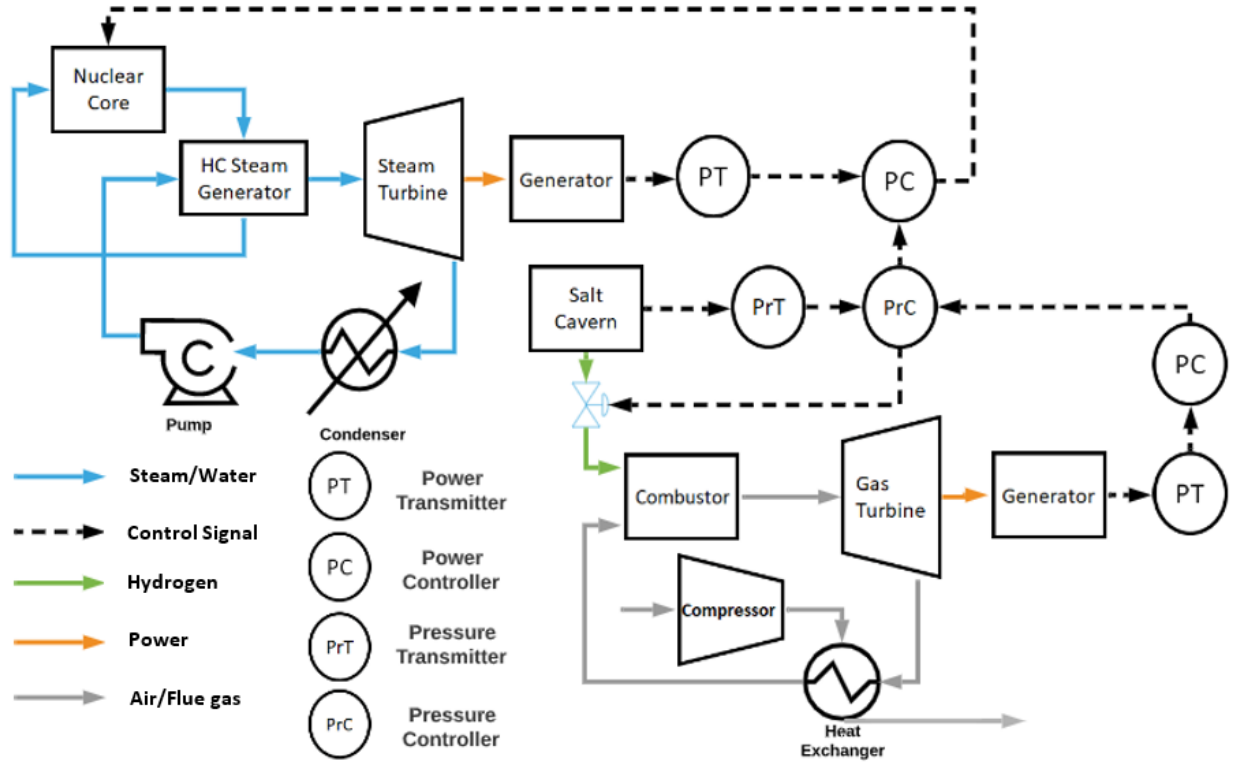


**Figure 2.** The control scheme of the proposed NHES.

PI controllers regulate the power output of the steam Rankine cycle as well as the gas turbine cycle. To moderate the power output of the steam Rankine cycle, the pressure inside the salt cavern is directly measured through a pressure sensor (PrT in Figure 2). When the pressure inside the salt cavern reaches its maximum limit, the hydrogen generation is stopped. If the grid demand is lower than the nominal capacity of the steam Rankine cycle, the power output of the steam Rankine cycle is ramped down and match with the grid demand by changing the control rods position. If the grid demand is higher than the nominal capacity of the steam Rankine cycle, no action needs to be taken, as there is no excess electricity used to generate hydrogen. This way, it is ensured that the salt cavern will operate within its safety conditions.

When the demand is higher than the nominal capacity of the steam Rankine cycle, the rest of the demand can be met with by the hydrogen gas turbine. The difference between the grid

demand and the steam cycle nominal capacity is the gas turbine set point. If the grid demand is lower than the steam cycle nominal capacity, the gas turbine set point is set to zero. The controller for the gas turbine will moderate the power output by changing the amount of hydrogen needed for fuel. There is also a pressure sensor for this controller. When the pressure inside the salt cavern reaches the minimum pressure threshold, the controller would shut down the gas turbine.

### **3.6 Model Validation**

The model validation is presented in the Supplementary Materials.

## **4. Results and Discussions**

This section presents the dynamic simulation results of the proposed NHES. Using the developed model and control schemes, the performance of the proposed NuScale NHES is evaluated by using data from New England ISO [55] for the system's grid demand, scaled down to the appropriate level. The NHES system is simulated over a one-year period, using grid data from October 2019 to October 2020. Even though the system is simulated for a whole year, the results are presented for the months of October, April - May, and July. The month of October is chosen as the representative results for the system when the hydrogen gas turbine cycle can provide extra electricity to the grid. This is the most common scenario in the study, occurring 92.6% of the year. The months of April and May are chosen because it shows the system's capability to ramp down the nuclear reactor when needed. The month of July is chosen to demonstrate the system controller's capability to shut down the gas turbine when the salt cavern is emptied.

To compare the results of the proposed hybrid system in this study with a stand-alone nuclear reactor, different performance criteria are chosen. These criteria include nuclear plant capacity factor, total power produced, percentage of total demand met, percentage of time when



the demand is met, total number of ramping cycles, standard deviation of the nuclear power output, and the percentage of time needed to ramp up and down.

Nuclear capacity factor is defined as the total output of the nuclear plant divided by the maximum total output of the nuclear plant. This is computed for both the NHES and stand-alone reactor by integrating the nuclear output over one-year and dividing by the maximum total power output. The total power produced is the total amount of electricity produced by all the electrical generators, which is just the nuclear plant in the case of a stand-alone nuclear plant, but also include the gas turbine output in the hybrid system. This is computed by integrating the total power output for both cases over a one-year period. The percentage of total demand met is calculated as the total power produced divided by the total demand from the grid during the time frame of the study

A full ramping cycle is defined in this paper as when the control rods of the nuclear reactor ramps down to a local minimum and then ramps back up to a local maximum. The total number of ramping cycles reveal how much the nuclear reactor has to ramp up and down and thus can be used to compare the flexible capacity of the two scenarios. The standard deviation of the nuclear power output is computed by finding the standard deviation of the nuclear power output for both systems. This is used to compare the amount of variation of the nuclear output, and thus demonstrate that the proposed NHES reduces the ramping rate. Lastly the percentage of time needed to ramp up and down is the amount of time the NHES and the stand-alone reactor ramp up and down, divided by one year. This criterion is chosen to show the impact on ramping rate the NHES has on a nuclear power plant.

#### **4.1 Results for Baseline Scenario (October)**

The simulation results of October 2019 are shown in Figure 3. It is assumed that at the beginning of the study, there is some hydrogen inside the salt cavern storage, and an initial pressure

is 10 MPa. It is shown at the end of the year-long study that this assumption is justified with the pressure returning to a higher value at the end of the year. The results presented in Figure 3 are as follows: 3 (a): the power output of the NHES, 3 (b): the control rods position of the nuclear reactor, and 3 (c): the pressure inside the salt cavern.

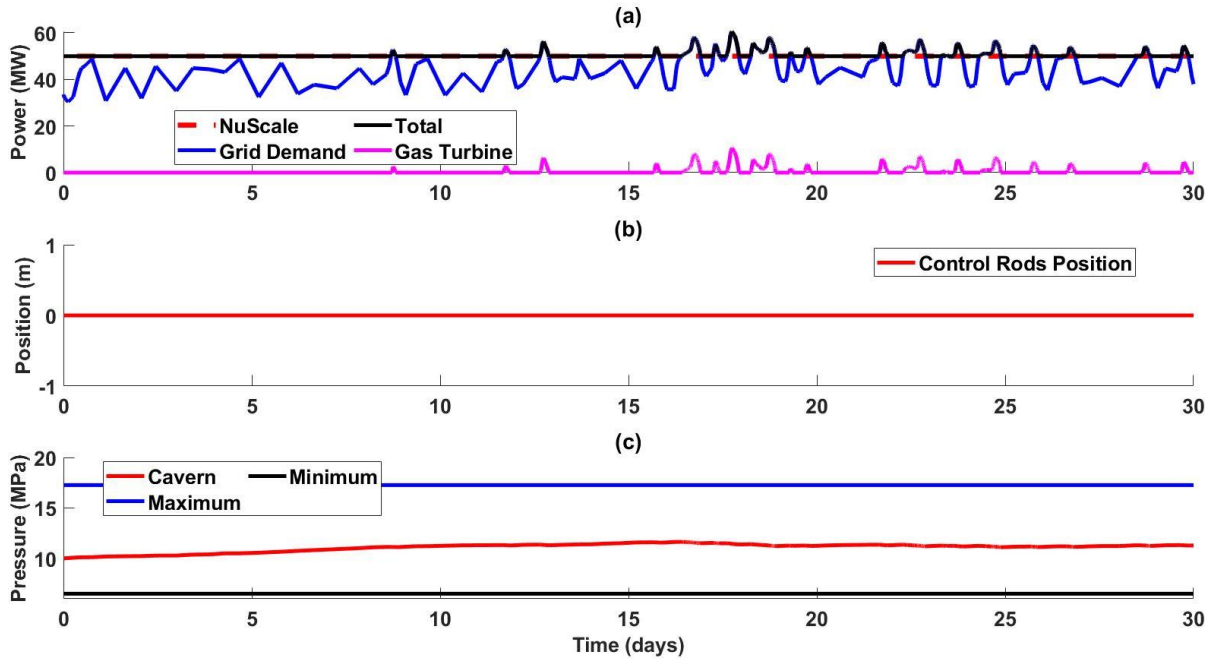


**Figure 3.** NHES simulation results for October 2019: (a) power output of NHES, (b) control rods position of the NuScale plant, and (c) pressure in salt cavern storage.

For 9 out of 12 months of the year, the results are similar to those of Figure 3. As shown in Figure 3 (a), the system is capable of meeting the demand with the addition of the gas turbine cycle when the demand is high. In the month of October, the grid demand fluctuates from 30.2 MW to 60.7 MW. There are 19 periods of time in October where the grid demand rises above the nominal capacity of the steam Rankine cycle. During these peak periods, the gas turbine cycle produces the additional electrical capacity to meet the grid demand. During the rest of the time when the grid demand is lower than the nominal capacity of the steam cycle, the excess electricity

is redirected towards the generation of hydrogen. This enables the NuScale plant to operate at baseload the whole month of October, as seen in Figure 3 (b), where the control rods position stays unchanged at 0 meters. The change in the hydrogen inside the storage can be seen in Figure 3 (c). At the beginning of October, the grid demand is lower than the nominal capacity of the steam Rankine cycle, which enables the excess energy to be used to generate hydrogen and be stored in the salt cavern. When the demand climbs, the hydrogen is taken out from the storage and used to fuel the gas turbine. In October, the amount of hydrogen generated is higher than the amount of hydrogen needed, leading to an increase in the hydrogen in the salt cavern. The pressure inside the salt cavern is increased from 10 MPa to 11.16 MPa for October.

From October 2019 to the first three weeks of May 2020, as well as the latter half of August and the whole month of September 2020, 100% of the total demand of the grid is met by the NHES. This is due to the addition of the storage element in the hydrogen generation and the salt cavern as well as the addition of the hydrogen gas turbine cycle. With the addition of these elements, the system is capable of increasing the nominal capacity compared to a stand-alone reactor from 49.95 MWe to 64 MWe, as well as increase the flexibility of the nuclear component.

To compare the results of the NHES and a stand-alone reactor, Figure 4 presents the simulation result of a stand-alone nuclear reactor. Figure 4 (a) shows the total demand of the grid as well as the power produced by the stand-alone reactor. Figure 4 (b) shows the positions of the control rods ramping up and down to regulate the amount of power produced by the nuclear reactor.

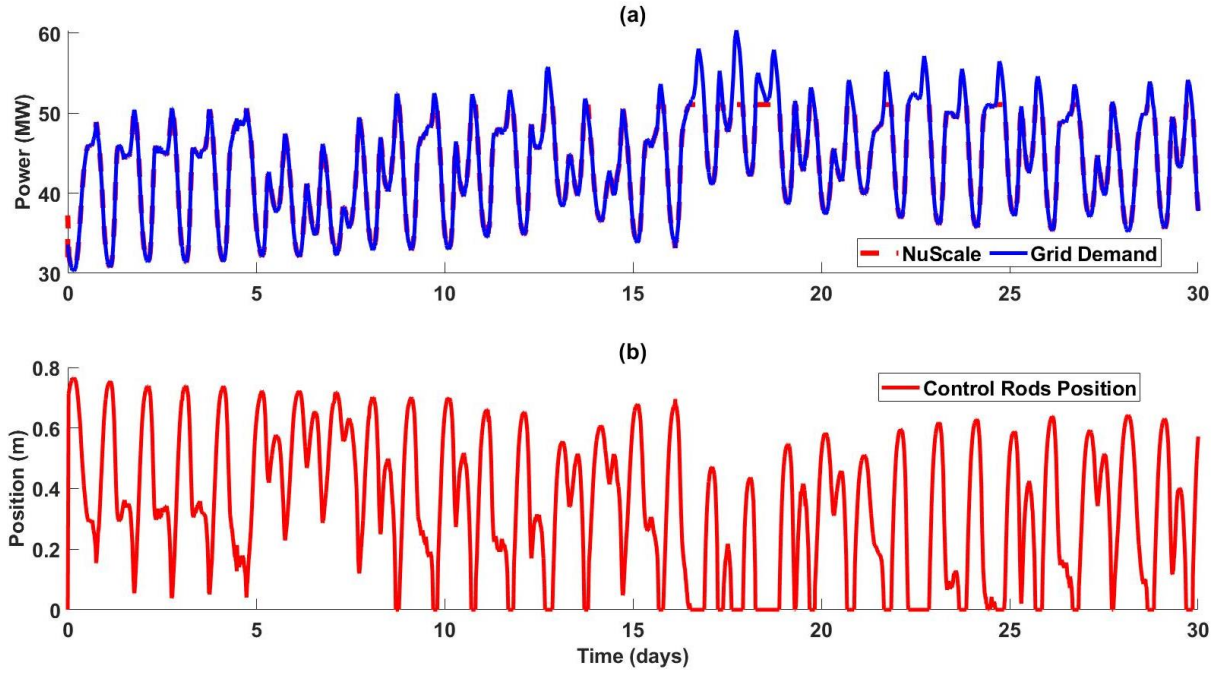


**Figure 4.** Stand-alone nuclear reactor simulation results for October 2019: (a) power output of the stand-alone NuScale plant, and (b) control rods position of the stand-alone NuScale plant

As can be seen in Figure 4 (a), the grid demand (shown in dashed blue lines) fluctuates from 30.2 MW to 60.7 MW. There are 19 periods covering 20.1% of the month in which the grid demand rises above the nominal capacity of the NuScale plant. In these instances, the plant is not capable of meeting the demand of the grid, making it a necessity to buy additional power from other electricity sources. This means that in this case study, for the month of October, the stand-alone NuScale plant is only capable of meeting the demand 79.9% of the time, compared to 100% of the time for the NHES. As can also be seen in both Figure 4 (a) and (b), when the demand is lower than the nominal capacity of the NuScale plant, the plant is forced to ramp down to not overload the grid with excess electricity. This causes a change in the control rods position, which is shown in Figure 4 (b). In the month of October, to follow the grid demand, there are 50 ramping

cycles compared to 0 for the NHES. In October, the stand-alone reactor produces 31.3 MWh, compared to 36.3 MWh produced by the NHES.

#### **4.2 Results for Energy Storage Build (April and May)**

The results for the month of April are presented in Figure 5 (a)-(c). In the winter months from October to April, the peak demand is not very high, thus the excess power generated from the nuclear reactor can be used to produce hydrogen. By April, the salt cavern reaches its maximum pressure, thus requiring the nuclear reactor to ramp down to not overwhelm the grid system. As seen from Figure 5 (c), the salt cavern reaches its maximum pressure on the 17<sup>th</sup> day. The reactor is ramped down by inserting the control rods into the nuclear reactor, as shown in Figure 5 (b). This happens because the steam Rankine cycle is capable of switching to flexible load-following operations as soon as the salt cavern reaches its maximum pressure threshold, as seen in Figure 5 (a). This ensures that the salt cavern does not exceed the safety standard. For the month of April, the grid demand fluctuates from 27.5 MW to 48.6 MW. Because the grid demand is lower than the nominal capacity of the steam Rankine cycle (49.95 MWe), the gas turbine cycle does not need to be operated. This means that the hydrogen inside of the salt cavern goes unused, and by the end of April, stays constant at the maximum level, as seen in Figure 5 (c). Because of the ramping, the nuclear reactor had 24 ramping cycles in the month of April, which can be seen in Figure 5 (b).

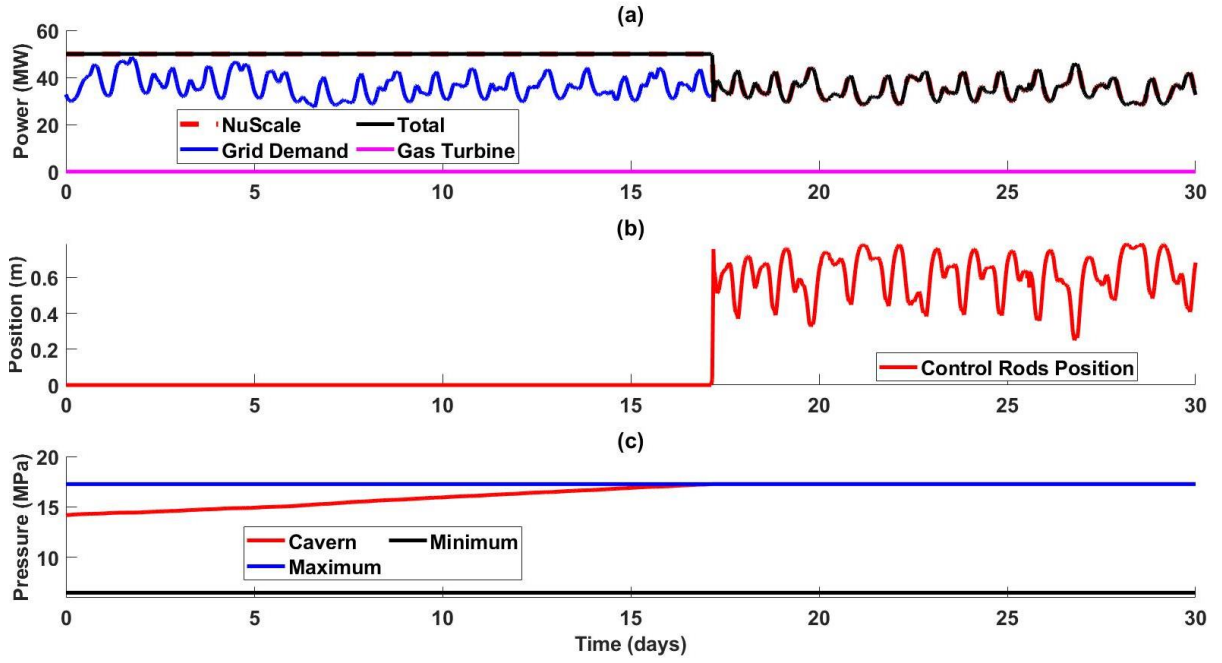


**Figure 5.** NHES simulation results for April 2020: (a) power output of NHES, (b) control rods position of the NuScale plant, and (c) pressure in salt cavern storage.

The results for May are illustrated in Figure 6 (a)-(c). As shown in Figure 6 (a), as the peak demand increases in May, the hydrogen in the pressure-constrained salt cavern is used to generate electricity and supply the demand peaks. However, as the hydrogen pressure reaches the upper limit a few times in the month of May as seen in Figure 6 (c), the nuclear reactor still has to ramp down when the storage is at the maximum pressure (Figure 6 (b)). However, as the gas turbine picks up at a few times this month, the hydrogen gets depleted which lessens the ramping for the nuclear reactor. For May, the nuclear reactor only has 15 ramping cycles. For this specific case study, the total amount of time the reactor is needed to ramp up and down to accommodate the grid demand is solely in April and May, and is only about 7.4% of the whole year. This allows the operator to plan, as they know the level of hydrogen inside the salt cavern. The ramping cycle can be further minimized by optimizing this hybrid system.

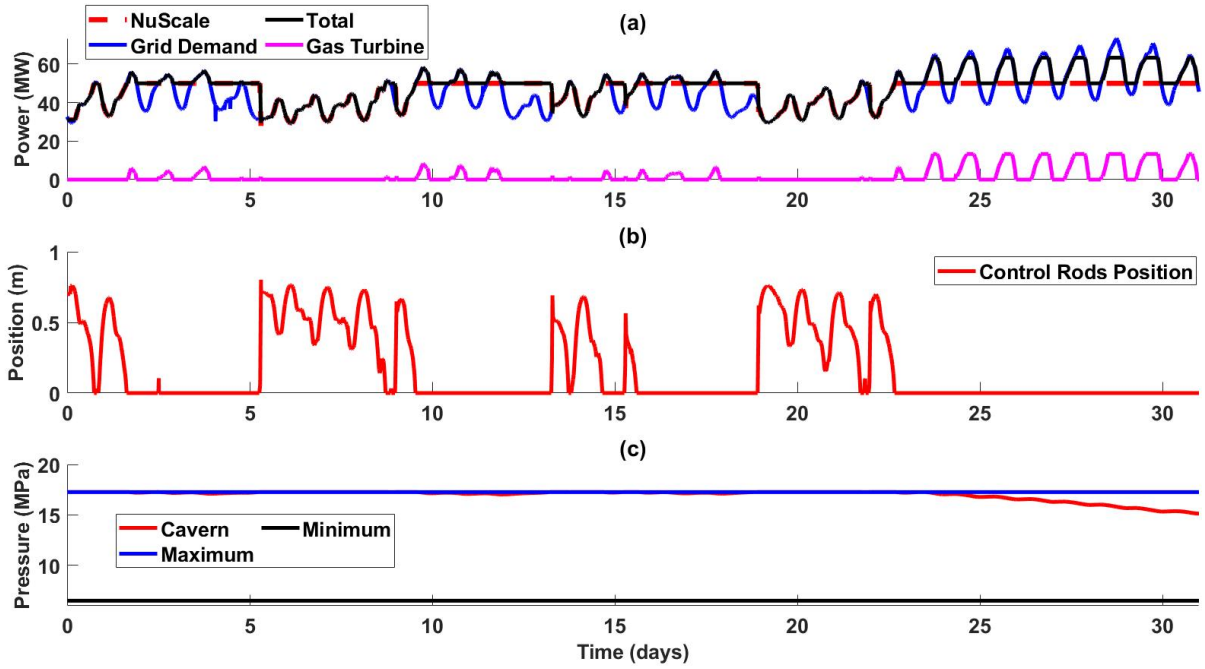


**Figure 6.** NHES simulation results for May 2020: (a) power output of NHES, (b) control rods position of the NuScale plant, and (c) pressure in salt cavern storage.

The results for April and May show the technical feasibility of the plant in a different operating condition than was shown in October. Specifically, the results for April and May show the reliable control for the steam Rankine cycle. The controller can ramp down the power output of the steam Rankine cycle to match with the grid demand when the salt cavern pressure maxes out.

The comparisons between the NHES and a stand-alone nuclear reactor for April and May are presented in the Supplementary Materials.

#### 4.3 Results for Peak Energy Use (July)

The simulation results for July are shown in Figures 7 (a)-(c). Summer months of June and July have the highest demand reaching 83.0 MW and 85.9 MW, respectively. To meet the high peak demand, the gas turbine cycle needed to be run often at its maximum capacity. The high

demand results in the gas turbine withdrawing hydrogen, as well as reducing the amount of hydrogen generated through excess electricity. As a result, the hydrogen is drained from the salt cavern.

As can be seen in Figure 7 (c), after the first 5 days in July, the hydrogen pressure inside the salt cavern reaches the minimum threshold and the storage becomes empty. Even though the storage gets refilled again as the grid demand dips below the nominal capacity of the steam Rankine cycle a few times, there is not enough hydrogen for the gas turbine to meet the peak demands for July. Figure 7 (a) and (c) shows that the gas turbine cycle shuts down when there is no more hydrogen in the salt cavern. As the salt cavern gets some more hydrogen, the gas turbine is capable of producing some electricity again, but not much. In this case study, for the month of July, the gas turbine cycle is only capable of producing 1.4 GWh. As the nuclear reactor is already operating in its maximum capacity, the system is not able to meet the grid demand, and other sources of electricity is needed to fulfill the rest of the electrical need. The total output of the NHES is 38.5 GWh, with 37.1 GWh coming from the steam Rankine cycle. The total grid demand for July is 41.5 GWh, meaning an additional 3 GWh needs to be bought from outside electricity sources.



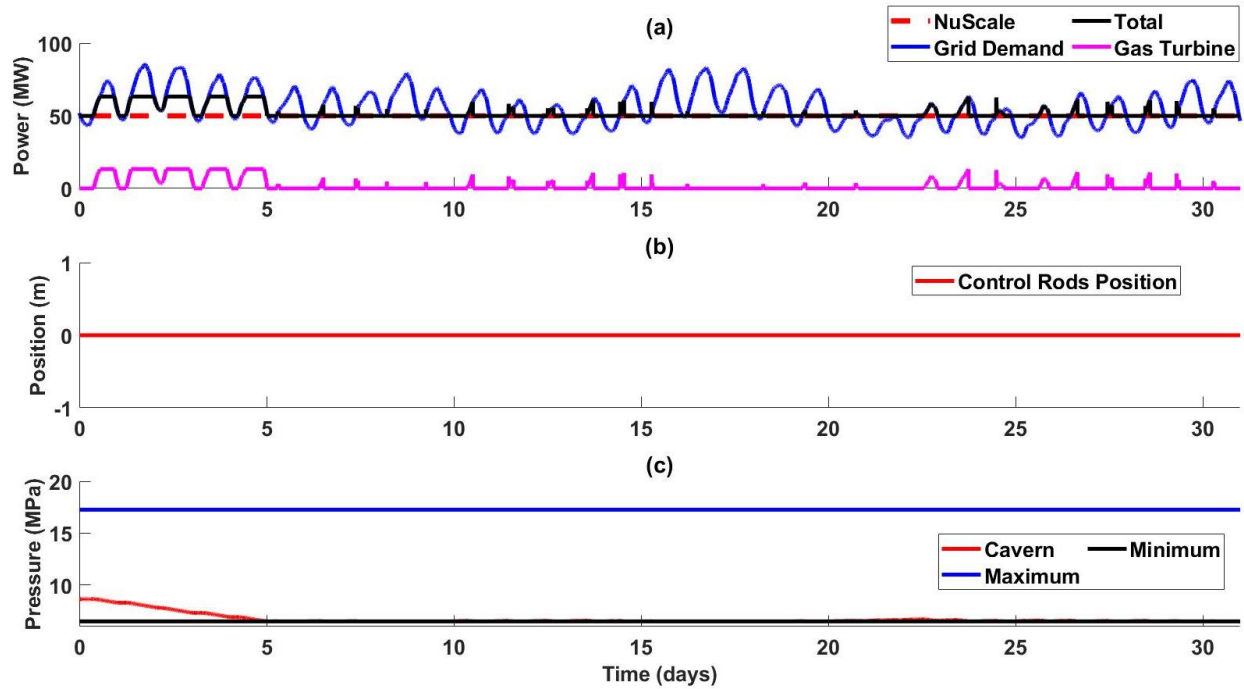


**Figure 7.** NHES simulation results for July 2020: (a) power output of NHES, (b) control rods position of the NuScale plant, and (c) pressure in salt cavern storage.

To compare the results of the NHES and a stand-alone reactor, Figure 8 presents the simulation result of a stand-alone nuclear reactor for July. As can be seen in Figure 8 (a), the grid demand fluctuates from 34.9 MW to 85.9 MW in July. There are 29 periods that cover 62.5 % of the months in which the grid demand is higher than the nominal capacity of the NuScale plant. For these cases, as the plant cannot meet the grid demand, it is necessary to purchase additional power from other sources. This means that for the month of July, the stand-alone NuScale plant can only supply 37.4% of the demand. As shown in Figures 8 (a) and 8 (b), when the demand is lower than the nominal capacity of the NuScale plant, the plant is forced to ramp down to not overload the grid with excess electricity. In the month of July, to follow the grid demand, there are 29 ramping cycles compared to 0 for the NHES. The stand-alone reactor produces 35.4 MWh in July, while the NHES produces 38.6 MWh.

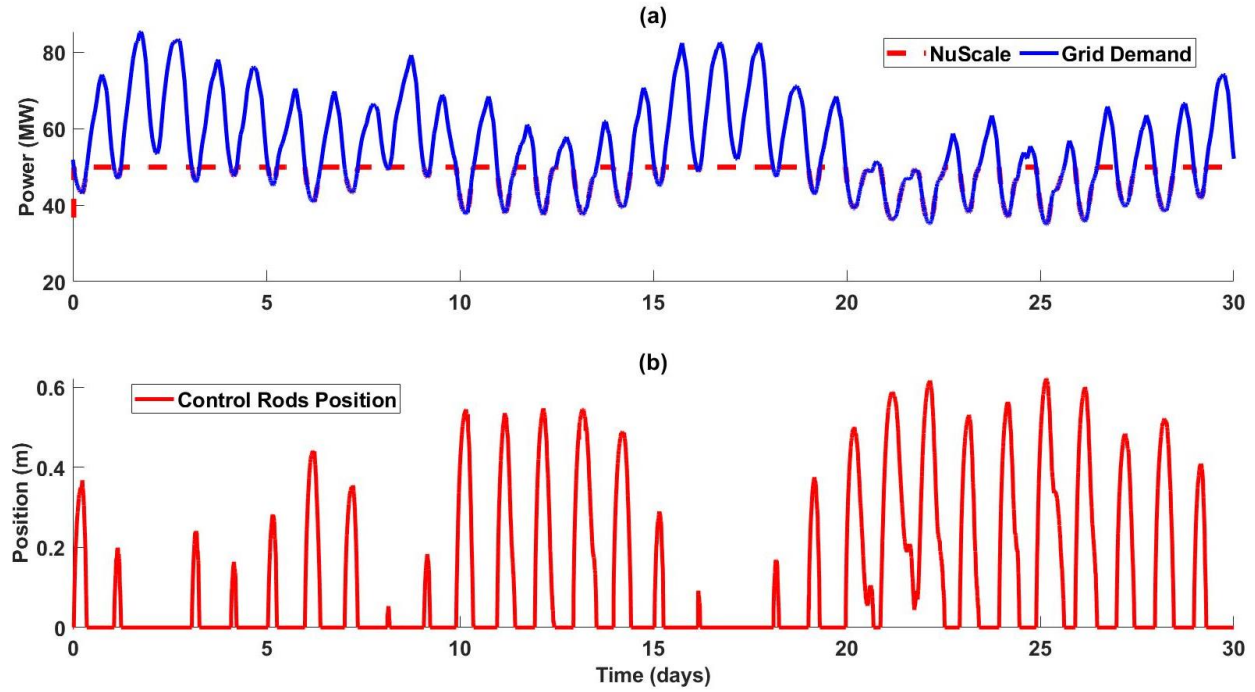


**Figure 8.** Stand-alone nuclear reactor simulation results for July 2020: (a) power output of the stand-alone NuScale plant, (b) control rods position of the stand-alone NuScale plant

This month is the worst-case scenario for the proposed hybrid system, as the amount of outside electricity is almost identical to the stand-alone nuclear reactor case. However, the nuclear reactor can continue to run at baseload, and there is no need for ramping up and down. The gas turbine can contribute some electricity as the salt cavern gets renewed. The gas turbine can also be used to run on natural gas instead of hydrogen as fuel, and thus drive down the cost of buying electricity from outside sources. In this worst-case scenario, it is still better than a stand-alone nuclear reactor, as it decreases the amount of ramping needed for the nuclear reactor, as well as the amount of electricity needed to buy to meet the grid demand.

The results for July also show the reliable control for the gas turbine cycle. As the hydrogen storage gets depleted, the controller is capable of shutting down the gas turbine cycle, thus ensuring

the salt cavern storage stays within its safety bounds. When there is hydrogen inside the salt cavern, the controller is capable of turning on the gas turbine cycle again.

#### 4.4 Comparison between the proposed NHES and a stand-alone reactor.

Figure 9 shows the comparison between the hybrid system and a stand-alone nuclear reactor, using a 7-day rolling average.

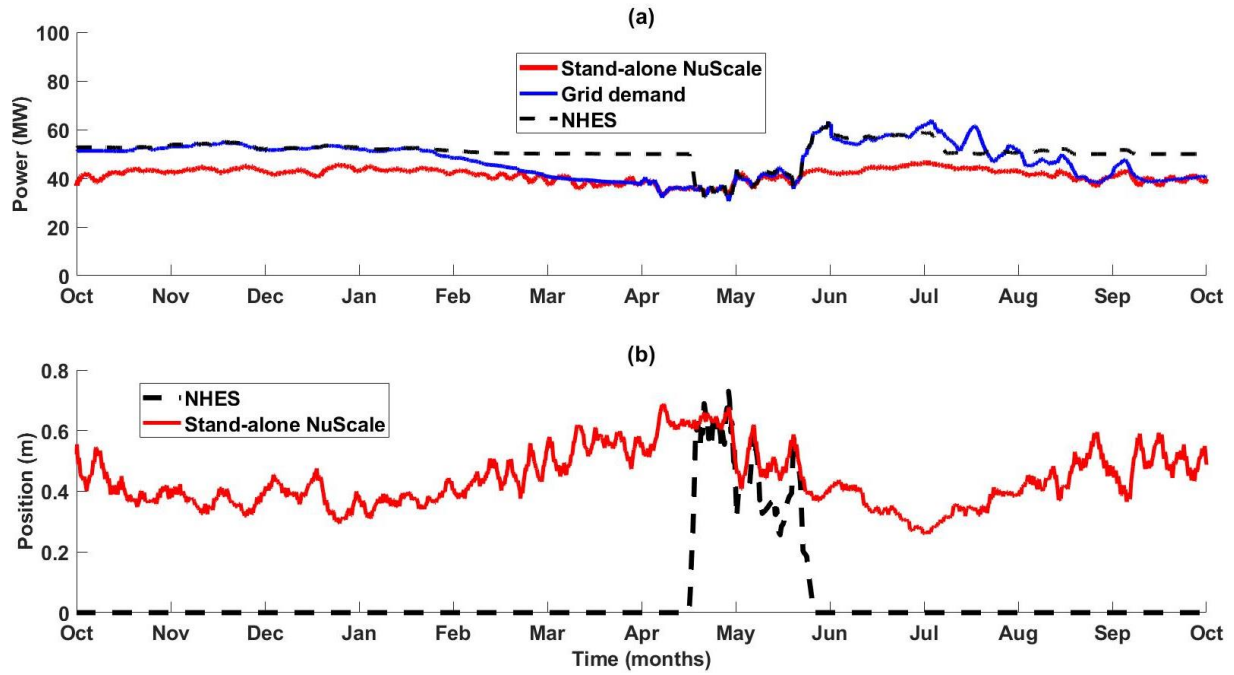


**Figure 9.** Year-long results for the NHES and stand-alone (7 day rolling average): (a) power output, (b) control rods position

A comparison between the proposed hybrid system with a standalone nuclear system demonstrates that the hybrid system is capable of load following while reducing the number of nuclear fuel rods thermal cycles. The hybrid system also has higher nuclear capacity factor, total power produced, percentage of total demand met, and reduces the number of ramping cycles. As shown in Figure 9 (a), a stand-alone nuclear reactor cannot fully meet the grid demand, and needs to rely on other sources of electricity to meet the demand. The proposed hybrid energy system is

capable of meeting the grid demand for the majority of the year except for June and July. Also, the proposed hybrid system doesn't have to constantly ramp up and down to not overload the grid system for the majority of the year. This allows the nuclear reactor to run at base load capacity, and only ramps up and down when the hydrogen storage is full.

Table 1 summarizes the results of the comparisons between the proposed hybrid system and a stand-alone reactor, with the criteria mentioned above. It is found that the NHES has a nuclear capacity factor of 98.3%, while a stand-alone plant has a capacity factor of 86.3%, showing that the hybrid system can increase the capacity factor around 12%. This increase is due to the fact that the nuclear reactor does not need to ramp down the production of electricity as often when the demand is low. The total power produced by the NHES is 443 GWh, while the stand-alone plant only generates 379 GWh, showing that the hybrid plant has 16.9% higher power production capacity. This is because the extra electricity produced during low demand period is used to produce and store hydrogen in the salt cavern. Later during the high demand time, the stored hydrogen is used to produce electricity using the gas turbine cycle, which increased the electricity production capacity. The proposed NHES is able to meet the grid demand without the need of outside electricity sources 93% of the year. Whereas the stand-alone nuclear power plant is not able to produce enough electricity to meet the demand once the demand rises above the nominal capacity of the nuclear plant. This means that the nuclear plant is capable of meeting the demand only 73.4% of the year.

The proposed NHES also drastically reduced the number of ramping cycles of the nuclear reactor, having only 39 ramping cycles over the course of one year. While the stand-alone reactor has 533 ramping cycles. This shows a 92.7% reduction over the period of a one year. The average power produced by the NuScale reactor in the proposed NHES is 49.38 MW with a standard

deviation of 0.878 MW, while the average power produced by a stand-alone plant is 43.34 MW with a standard deviation of 5.50 MW. This shows that the standard deviation of the stand-alone plant is almost 6 times higher than the hybrid system. This is due to the fact that the nuclear reactor in the proposed hybrid system only has to ramp up and down 7.4% of the year, meaning that the reactor is allowed to run at 100% capacity 92.6% of the year. Whereas a stand-alone nuclear reactor would have to be constantly ramping up and down throughout the whole entire year without any breaks. This shows the proposed NHES's ability to drastically reduce the ramping rate of a nuclear power plant, while increases the flexibility and capability to load follow.

**Table 1**

Summary table of comparison between NHES and stand-alone plant.

| Parameters                                 | NHES              | Stand-alone plant |
|--------------------------------------------|-------------------|-------------------|
| Nuclear capacity factor                    | 98.3%             | 86.3%             |
| Total power produced (MWh)                 | $443 \times 10^3$ | $379 \times 10^3$ |
| Percentage of total demand met             | 98%               | 95%               |
| Percentage of time when demand is met      | 93%               | 73.4%             |
| Total number of cycles                     | 39                | 533               |
| Standard deviation of nuclear power output | 0.808 MW          | 5.50 MW           |
| Percentage of time ramping up and down     | 7.4%              | 100%              |

#### 4.5 Year-long simulation results

The results of the year-long simulation of the NHES study, with 7-day rolling average are shown in Figure 10 (a)-(c).

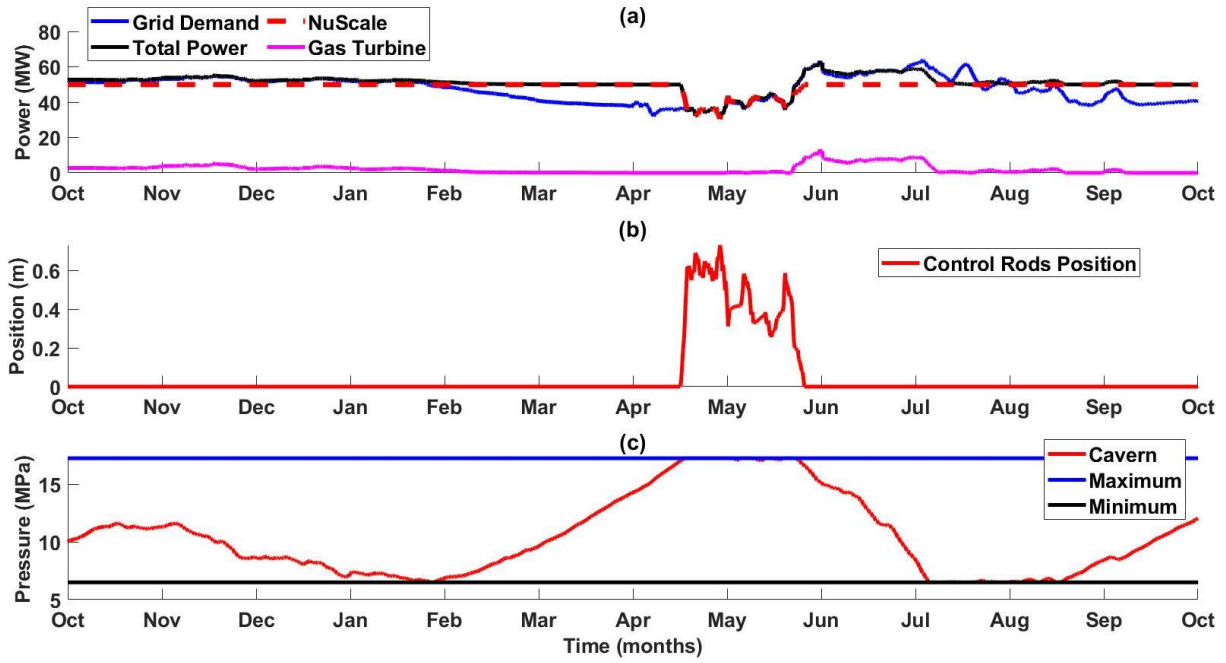


**Figure 10.** Year-long simulation results for the NHES study: (a) power output, (b) control rods position, (c) salt cavern pressure

According to Figure 10 (a), the NHES is capable of flexibly providing the required electricity to the grid demand throughout the whole year. The grid demand, shown by the dashed red line, is shown to be below the total NHES power produced (blue line) 93% of the year. This means that in 93% of the year in this case study, the NHES can supply enough electricity to the grid without the addition of outside sources. This includes the times when the grid demand rises above the nominal capacity of the steam Rankine cycle (shown by the black dashed line). This is due to the addition of the storage as well as the hydrogen gas turbine (shown by the pink line). The storage elements are used to convert excess electrical energy from the steam Rankine cycle into hydrogen and store it long term in an underground salt cavern. The hydrogen gas turbine cycle is used to produce additional electricity using the stored hydrogen inside the salt cavern. 7 % of

the year is shown where the grid demand rises above the total power produced. This is because at this time, the stored hydrogen is emptied, and the gas turbine cycle is shut down.

Figure 10 (b) shows the stability of the nuclear power plant, only needing to ramp 7.4% of the year. This is because of the flexibility added due to the addition of the hydrogen generation plant and the large-scale hydrogen storage in the underground salt cavern. Without these additions, the nuclear plant would have to ramp up and down the whole year, which would increase the cost of operation of the nuclear plant, as well as the degradation of the fuel. By adding the storage capacity in the form of hydrogen, the proposed NHES is capable of flexibly operating in a highly oscillating grid environment, where the lowest demand can be as low as 27.5 MWe to the highest demand of 85.9 MWe.

Figure 10 (c) shows that the salt cavern is capable of replenishing itself every year. It is assumed at the beginning of the case study that there was hydrogen inside the salt cavern, with its starting pressure at 10 MPa. By the end of the case study, it is shown that the salt cavern refilled itself, with ending pressure at 12.25 MPa.

The year-long results show the reliability of the controllers used in the study. As the grid demand fluctuates from 27.5 MWe to 85.9 MWe, the control system is capable of meeting the grid demand by either changing the control rods position of the nuclear reactor, or the amount of hydrogen as fuel for the gas turbine cycle. The controller is also capable of taking in the pressure inside the salt cavern. When the salt cavern is full, the control system is capable of ramping down the output of the steam Rankine cycle by inserting the control rods into the nuclear reactor. In the months of April and May, the salt cavern's pressure reaches its maximum threshold as shown in Figure 10 (c). At that time, the control rods were inserted into the nuclear reactor, as shown in Figure 10 (b). When the salt cavern is no longer full, the control system allows the nuclear reactor

to run at base load capacity (control rods position at 0 meters in Figure 10 (c)). When the salt cavern is emptied, the control system is capable of shutting down the gas turbine cycle. As shown in Figure 10 (c), when the salt cavern is emptied during the months of July and August, the gas turbine cycle is shut down, as shown in Figure 10 (a).

## **5. Conclusions**

A one-year case study of a nuclear hydrogen hybrid energy system with large scale storage in salt cavern was performed to assess the technical feasibility and the benefits of such system. To perform the study, real grid demand data was taken from ISO New England, scaled from a regional profile to a demand profile of a city.

The proposed hybrid system was capable of load following while minimizing the load cycles of the nuclear reactor. This was due to the addition of the hydrogen generation plant, as well as a large-scale energy storage in the form of an underground salt cavern. By adding these buffers to the system, the flexibility of the system increased without the negative side effects of flexibly operating a nuclear power plant. These additions enabled the nuclear power plant to run at base load 92.6% of the year. The hybrid system also helped to reduce the number of ramping cycles by 92.7% over a one-year period from 533 ramping cycles to 39 ramping cycles. This improved the profitability of the plant and reduced the risk of the mechanical and thermal fractures on the fuel and the cladding inside the plant. The addition of the hydrogen gas turbine enabled the hybrid system to generate more than the maximum capacity of the nuclear power plant, which increased the nominal capacity of the system and the total amount of power produced. The amount of power produced by the hybrid plant increased by 16.9% compared to a stand-alone plant over the course of a year (an increase from 379 GWh to 443 GWh). Due to the addition of the gas turbine cycle, the hybrid system could supply the grid demand for 93% of the year, whereas a stand-alone nuclear



plant could meet the demand for 73.4% of the year. The addition of the hydrogen generation system, the large-scale hydrogen storage, and the hydrogen electricity generation caused an increase of almost 20% in the supplied demand.

Future studies should be conducted to optimize the dispatch of nuclear power production and energy storage through an economic analysis.

### **Acknowledgement**

The authors are grateful for the funding sources provided by Department of Energy's Nuclear Energy University Program under Grant Number DE-NE0008866.

## References

- [1] R. Pinsky, P. Sabharwall, J. Hartvigsen and J. O'Brien, "Comparative review of hydrogen production technologies for nuclear hybrid energy systems," *Progress in Nuclear Energy*, 2020.
- [2] S. Moataz and K. Powell, "Using Real-Time Electricity Prices to Leverage Electrical Energy Storage and Flexible Loads in a Smart Grid Environment Utilizing Machine Learning Techniques," *Processes*, vol. 7, 2019.
- [3] S. Moataz, K. Mohammadi and K. Powell, "Techno-economic analysis of the impact of dynamic electricity prices on solar penetration in a smart grid environment with distributed energy storage," *Applied Energy*, vol. 282, 2021.
- [4] M. R. Abdussami, M. I. Adham and H. A. Gabbar, "Modeling and performance analysis of nuclear-renewable micro hybrid energy system based on different coupling methods," *Energy Reports*, vol. 6, pp. 189-206, 2020.
- [5] J. F. Tuttle and K. M. Powell, "Analysis of a thermal generator's participation in the Western Energy Imbalance Market and the resulting effects on overall performance and emissions," *The Electricity Journal*, vol. 32, no. 5, pp. 38-46, 2019.
- [6] A. Epiney, C. Rabiti, P. Talbot and A. Alfonsi, "Economic analysis of a nuclear hybrid energy system in a stochastic environment including wind turbines in an electricity grid," *Applied Energy*, 2020.
- [7] S. Moataz, K. Mohammadi and K. Powell, "Solving the duck curve in a smart grid environment using a non-cooperative game theory and dynamic pricing profiles," *Energy Conversion and Management*, vol. 220, 2020.
- [8] J. S. Kim, K. M. Powell and T. F. Edgar, "Nonlinear Model Predictive Control for a Heavy-Duty as Turbine Power Plant," in *American control conference*, Washington D.C., 2013.
- [9] B. S. Palmintier and M. D. Webster, "Impact of operational flexibility on generation planning with renewable and carbon targets," *IEEE Trans Sustain Energy*, 2016.
- [10] F. J. Sisternes, J. D. Jenkins and A. Botterud, "The value of energy storage in decarbonizing the electricity sector," *Applied Energy*, 2016.
- [11] S. Suman, "Hybrid nuclear-renewable energy systems: A review," *Journal of Cleaner Production*, 2018.
- [12] J. D. Jenkins, Z. Zhou, R. Ponciroli, R. B. Vilim, F. Ganda, F. de Sisternes and A. Botterud, "The benefits of nuclear flexibility in power system operations with renewable energy," *Applied Energy*, 2018.

- [13] C. Forsberg, "Meeting Low-Carbon Industrial Heat Demand with High-Temperature Reactors Using Co-Generation and Heat Storage, Vol. 120," *Transactions of the American Nuclear Society*, 2019.
- [14] J. H. Keppler and M. Cometto, "Nuclear energy and renewables: system effects in low-carbon electricity systems.," *Nuclear Energy Agency*, 2012.
- [15] H. Ludwig, T. Salnikova, A. Stockman and U. Waas, "Load cycling capabilities of German Nuclear Power Plants (NPP).," *Int J Nucl Power*, 2010.
- [16] D. Machalek and K. Powell, "Automated electrical demand peak leveling in a manufacturing facility with short term energy storage for smart grid participation," *Journal of Manufacturing Systems*, vol. 52, pp. 100-109, 2019.
- [17] D. Machalek, A. Young, L. Blackburn, P. Rogers and K. M. Powell, "Mine operations as a smart grid resource: Leveraging excess process storage capacity to better enable renewable energy sources," *Minerals Engineering*, vol. 145, p. 106103, 2020.
- [18] P. Brimley, D. Machalek and K. Powell, "Smart Scheduling of a Batch Manufacturer's Operations by Utilization of a Genetic Algorithm to Minimize Electrical Demand," *Smart and Sustainable Manufacturing Systems*, vol. 3, no. 2, p. 20190018, 2019.
- [19] P. Nikolaidis and A. Poullikkas, "A comparative overview of hydrogen production processes," *Renew. Sustain. Energy Rev*, 2017.
- [20] M. El-Shafie, S. Kambara and Y. Hayakawa, "Hydrogen production technologies overview," *J. Power Energy Eng*, 2019.
- [21] International Energy Agency, "The Future of Hydrogen," Paris, 2019.
- [22] B. Sedaee, M. Mohammadi, L. Esfahanizadeh and Y. Fath, "Comprehensive modeling and developing a software for salt cavern underground gas storage," *Journal of Energy Storage*, 2019.
- [23] D. G. Caglayan, N. Weber, H. Heinrichs, J. Linßen, M. Robinius, P. A. Kukla and D. Stolten, "Technical Potential of Salt Caverns for Hydrogen Storage in Europe," *International Journal of Hydrogen Energy*, 2020.
- [24] H. Landinger, and F. Crostogino, "The role of large-scale hydrogen storage for future renewable energy utilisation," *Second International Renewable Energy Storage Conference*, 2007.
- [25] OFFICE of FOSSIL ENERGY, U.S. Department of Energy, "Strategic Petroleum Reserve," 2021.
- [26] Y. Wang, J. Kowal, M. Leuthold and D. U. Sauer, "'Storage System of Renewable Energy Generated Hydrogen for Chemical Industry," *Energy Procedia*, pp. 657-667, 2012.
- [27] D. T. Ingersoll, Z. J. Houghton, R. Bromm, and C. Desportes, "NuScale small modular reactor for Co-generation of electricity and water," *Desalination*, 2014.

- [28] B.-c. Zhao, M.-s. Cheng, C. Liu and Z.-m. Dai, "Conceptual design and preliminary performance analysis of a hybrid nuclear-solar power system with molten-salt packed-bed thermal energy storage for on-demand power supply," *Energy Conversion and Management*, 2018.
- [29] R. S. El-Emam, H. Ozcan and C. Zamfirescu, "Updates on promising thermochemical cycles for clean hydrogen production using nuclear energy," *Journal of Cleaner Production*, 2020.
- [30] S. Şahin and H. M. Şahin, "Generation-IV reactors and nuclear hydrogen production," *International Journal of Hydrogen Energy*, 2021.
- [31] J. E. O'Brien, M. G. McKellar, E. A. Harvego and C. M. Stoots, "High-temperature electrolysis for large-scale hydrogen and syngas production from nuclear energy – summary of system simulation and economic analyses," *Int J Hydrogen Energy*, 2010.
- [32] NRC, "Design Certification Application - NuScale," December 2020. [Online]. Available: <https://www.nrc.gov/reactors/new-reactors/smr/nuscale.html>.
- [33] D. S. Falcao and A. Pinto, "A review on PEM electrolyzer modelling: Guidelines for beginners," *Journal of Cleaner Production*, 2020.
- [34] Modern Power Systems, "Gas turbines in the US are being prepped for a hydrogen-fuelled future," *NS Energy*, 6 Jan 2021.
- [35] MathWorks Inc., "MATLAB and Statistics Toolbox Release 2020b," MathWorks Inc., Natick, MA, USA, 2020.
- [36] A. Gabor, C. Fazeska and K. M. Hangos, "Modeling and Identification of a Nuclear Reactor with Temperature Effects and Xenon poisoning," in *IEEE Xplore*, 2009.
- [37] M. Johnson, S. Lucas and P. Tsvetkov, "Modeling of Reactor Kinetics and Dynamics," INL, Idaho Falls, 2010.
- [38] K. Frick, "Status Report on the NuScale Module Developed in the Modelica Framework," Idaho National Lab, 2019.
- [39] A. Sadegh-Noedoost, F. Faghihi, A. Fakhraei and M. Amin-Mozafari, "Investigations of the fresh-core cycle-length and the average fuel depletion analysis of the NuScale core," *Annals of Nuclear Energy*, vol. 136, February 2020.
- [40] D. L. Hetrick, *Dynamics of Nuclear Reactors*, USA: American Nuclear Society, 1993.
- [41] F. D'Auria, *Thermal-Hydraulics of Water Cooled Nuclear Reactors*, Woodhead Publishing, 2017.
- [42] F. Marangio and M. G. L. Santarelli, "Theoretical model and experimental analysis of a high pressure PEM water electrolyser for hydrogen production," *International Journal of Hydrogen Energy*, pp. 1143-1158, 2009.

- [43] T. Yigit and O. F. Selamet, "Mathematical modeling and dynamic Simulink simulation of high-pressure PEM electrolyzer system," *International Journal of Hydrogen Energy*, pp. 13901-13914, 2016.
- [44] M. M. Tomadakis and S. V. Sotirchos, "Ordinary and transition regime diffusion in random fiber structures," *AIChE Journal*, 1993.
- [45] M. Santarelli, "idrogeno e celle a combustibile".
- [46] M. G. L. Santarelli, M. F. Torchio and P. Cochis, "Parameters estimation of a PEM fuel cell polarization curve and analysis of their behavior with temperature," *Journal of Power Sources*, pp. 824-835, 2006.
- [47] J. C. Amphlett, R. M. Baumert, R. F. Mann, B. A. Peppley, P. R. Roberge and T. J. Harris,, "Performance modelling of the ballard mark iv solid polymer electrolyte fuel cell," *Journal of The Electrochemical Society*, vol. 142, 1995.
- [48] J. H. Nam and M. Kaviany, "Effective diffusivity and water-saturation distribution in single- and two-layer PEMFC diffusion medium," *International Journal of Heat and Mass Transfer*, vol. 46, no. 24, pp. 4595-4611, 2003.
- [49] Rajeshwar, M. Krishnan and L. Robert, *Solar hydrogen generation, toward a renewable energy future*, Springer, 2008.
- [50] F. Incropera, D. DeWitt, T. Bergman and A. Lavine, *Fundamentals of Heat and Mass Transfer*, John Wiley & Sons, 2006.
- [51] E. W. Lemmon, M. L. Huber and J. W. Leachman, "Revised Standardized Equation for Hydrogen Gas Densities for Fuel Consumption Applications," *Journal of Research of the National Institute of Standards and Technology*, vol. 113, no. 6, p. 341–350, 1 December 2008.
- [52] A. Witkowski, A. Rusin, M. Majkut and K. Stolecka, "Comprehensive analysis of hydrogen compression and pipeline transportation from thermodynamics and safety aspects," *Energy*, vol. 141, pp. 2508-2518, 15 December 2017.
- [53] HyUnder, "Assessment of the potential, the actors and relevant business cases for large scale and seasonal storage of renewable electricity by hydrogen underground storage in Europe," 2014.
- [54] M. Henning, D. Machalek and K. Powell, "Integrating a Microturbine into a Discrete Manufacturing Process with Combined Heat and Power Using Smart Scheduling and Automation," *Computer Aided Chemical Engineering*, vol. 47, pp. 293-298, 2019.
- [55] ISO New England, "Energy, Load, and Demand Reports," 2021.

## **Supplemental Materials**

### **Dynamic simulation of a novel nuclear hybrid energy system with large-scale hydrogen storage in an underground salt cavern**

**<sup>1</sup>An Ho, <sup>1</sup>Kasra Mohammadi, <sup>2</sup>Matthew Memmott, <sup>2</sup>John Hedengren, <sup>1,3</sup>Kody M. Powell**

<sup>1</sup>University of Utah, Department of Chemical Engineering, 50 South Central Campus Dr., 3290  
MEB, Salt Lake City, UT 84112-9203, USA

<sup>2</sup>Brigham Young University, Department of Chemical Engineering, Engineering Building,  
Provo, UT 84602, USA

<sup>3</sup>University of Utah, Department of Mechanical Engineering, 1495 E 100 S, Salt Lake City, UT  
84112, USA

# 1. Supplemental Theoretical Model

## 1.1 The Nuclear Reactor Model

The dynamic model for the nuclear reactor is adopted from [1] and [2]. The following assumptions are made for the modeling of the nuclear reactor [1]:

- The dynamic model of the reactor is based on the point kinetics equations
- The reactor is assumed to be spatially homogenous
- A single group of delayed neutrons is assumed
- The elements of the reactor consist of the fuel, the moderator, and the control rods
- The effect of control rods position on reactivity is assumed to be quadratic [1]
- The mass flow rate of the coolant is assumed to be constant [3]
- The reactivity dependence on the fuel and moderator temperature are assumed to be linear
- The heat loss of the reactor is assumed to be negligible

The input of the model is the control rods position, measured in meters. The length is correlated to the model that is used, so that it can be used to access the impact on the neutronics more clearly. The output of the model is the thermal power of the nuclear reactor (MWth) as well as the temperature of the moderator and the fuel.

### Neutron dynamics model of the reactor:

The neutron dynamics model is taken from [2]:

$$\frac{dn_{neu}}{dt} = \frac{\rho_{nuc}(t) - \beta_{mix}}{\Lambda} n_{neu}(t) + \lambda C_{neu}(t) \quad (1)$$

$$\frac{dC_{neu}}{dt} = \frac{\beta_{mix}}{\Lambda} n_{neu}(t) - \lambda C_{neu}(t) \quad (2)$$

where  $n_{neu}$  is the neutron density,  $\rho(t)$  is reactivity,  $\beta_{mix}$  is the effective delayed neutron fraction,  $\Lambda$  is the neutron generation time,  $\lambda$  is the decay constant for the single average group of delayed neutrons,  $C(t)$  is the concentration of the single average group of delayed neutrons. The values of  $\beta_{mix}$ ,  $\lambda$ , and  $\Lambda$  are given in Table 1.

**Table 2**

The values for the parameters in the neutron dynamic model.

| Parameter (unit)  | Value                 |
|-------------------|-----------------------|
| $\beta_{mix}$     | 0.0065                |
| $\lambda(s^{-1})$ | 0.07728               |
| $\Lambda(s)$      | $2.18 \times 10^{-5}$ |

The reactivity of the reactor is modelled using the following equation [1]:

$$\rho_{nuc}(t) = \alpha_f(T_f - T_{f0}) + \alpha_m(T_m - T_{m0}) + p_2 z^2 + p_1 z + p_0 \quad (3)$$

where  $T_f$  is the fuel temperature,  $T_m$  is the moderator temperature,  $T_{f0}$  and  $T_{m0}$  are the reference temperature of fuel and moderator respectively,  $\alpha_f$  is the fuel temperature feedback coefficient,  $\alpha_m$  is the moderator temperature feedback coefficient,  $z$  is the control rods position measured in meters,  $p_2 z^2 + p_1 z + p_0$  describes the effect of the control rods position to the reactivity. The values for the feedback coefficients are taken from [4] which is specifically for a NuScale reactor. The values for  $p_2$ ,  $p_1$ ,  $p_0$  are taken from [1], which is for a pressurized water reactor. The values for these parameters are given in Table 2.

**Table 3**

Values of parameters for reactivity calculation.

| Parameter (unit) | Value |
|------------------|-------|
|------------------|-------|



|                                       |                        |
|---------------------------------------|------------------------|
| $\alpha_f(\Delta k/k/^\circ\text{C})$ | $-1.98 \times 10^{-5}$ |
| $\alpha_m(\Delta k/k/^\circ\text{C})$ | $-28.2 \times 10^{-5}$ |
| $p_2$                                 | $-0.966$               |
| $p_1$                                 | $-0.44$                |
| $p_0$                                 | $0.0401$               |

#### Thermodynamic equations of the reactor:

To model the temperature of the fuel and coolant, energy balances are used. The energy balance on the fuel rods is as follow:

$$\frac{dT_f}{dt} = -\frac{hA_s}{\rho_f V_f C_{pf}}(T_f - T_m) + \frac{W_{therm}}{\rho_f V_f C_{pf}} \quad (4)$$

where  $\rho_f$  is the fuel density,  $V_f$  is the fuel volume,  $C_{pf}$  is the heat capacity of the fuel,  $W_{therm}$  is the thermal power generated from the fuel,  $h$  is the convective heat transfer coefficient from the fuel to the coolant,  $A_s$  is the surface area between the fuel and the coolant,  $\rho_f V_f C_{pf} \frac{dT_f}{dt}$  describes the inner energy change of the fuel due to temperature change, and  $hA_s(T_f - T_m)$  describes the transferred heat from the fuel to the coolant.

The energy balance on the coolant is:

$$\frac{dT_m}{dt} = \frac{hA_s}{\rho_m V_m C_{pm}}(T_f - T_m) - \frac{\dot{m}_m}{\rho_m V_m}(T_m - T_{m,in}) \quad (5)$$

where  $\rho_m$  is the coolant density,  $V_m$  is the coolant volume,  $C_{pm}$  is the heat capacity of the coolant,  $\rho_m V_m C_{pm} \frac{dT_m}{dt}$  describes the inner energy change of the coolant due to temperature change,  $\dot{m}_p$  is the coolant mass flow rate,  $T_{m,in}$  is the coolant inlet temperature.

The thermal power of the reactor is related to the neutron density as follows [5]:

$$W_{therm} = n_{neu}(t) \sigma_f^{235} E_f N_{235} V_{core} \quad (6)$$

where  $E_f$  is the average recoverable energy per fission,  $\sigma_f^{235}$  is the microscopic cross section of Uranium 235,  $N_{235}$  is the atomic number density of Uranium 235 in the fuel,  $V_{core}$  is the total volume of the core.

The convective heat transfer is calculated using the Dittus-Boelter correlation [6]:

$$h_{conv} = \frac{Nu_{Dh} \kappa_m}{Dh} \quad (7)$$

$$Nu_{Dh} = 0.023 Re_{Dh}^{0.8} Pr^{0.4} \quad (8)$$

where  $\kappa_m$  is the thermal conductivity of the coolant,  $Dh$  is the hydraulic diameter (m),  $Re$  is the Reynolds number of the flow,  $Pr$  is the Prandtl number, and  $Nu$  is the Nusselt number.

#### Steam generator

A steady-state energy balance on the steam generator is used:

$$\dot{m}_{steam} \Delta H_{steam} = \dot{m}_m C_{pm} (T_{m,in} - T_{m,out}) \quad (9)$$

The nominal value of steam flow rate is 67.6 kg/s at 580.9 K. According to [3], it is assumed that the steam generator exit temperature is constant. As the power output of the nuclear reactor changes, so does the temperature of the coolant. The amount of steam is calculated with new values of coolant temperature.

#### Steam Rankine cycle

The Rankine Cycle is modeled using pseudo-steady-state energy models. The power generated by the turbine is calculated using the following steady-state equation:

$$\dot{W}_{turb} = \dot{m}_{steam} (H_{turb,in} - H_{turb,out}) \quad (10)$$

Assuming that the turbine isentropic efficiency is constant, the enthalpy of the outlet steam of the turbine is calculated using Eq. (11) as follows:

$$H_{turb,out} = H_{turb,in} + \eta_{turb}(H_{turb-is,out} - H_{turb,in}) \quad (11)$$

where  $H_{turb-is,out}$  is the isentropic (ideal) outlet enthalpy of the steam.

The power needed for the pump is calculated using Eq. (12) as follows:

$$\dot{W}_{pump} = \dot{m}_{steam} \hat{V}_s (P_{pump,out} - P_{pump,in}) \quad (12)$$

where  $\hat{V}_s$  is the specific volume of water at the pump inlet conditions.  $P_{pump,out}$  is the pressure at the outlet of the pump, and  $P_{pump,in}$  is the pressure at the inlet of the pump.

## 1.2 Hydrogen Generation Model

### 1.2.1 Anode Module

The half-cell reaction taking place inside the anode is:



The oxygen flow rate is calculated as:

$$\dot{N}_{O_2} = \dot{N}_{O_2,an,in} - \dot{N}_{O_2,an,out} + \dot{N}_{O_2,gen} \quad (14)$$

$$\dot{N}_{O_2,gen} = \frac{I}{4F} \quad (15)$$

where  $I$  is the current, and  $F$  is Faraday's constant.

The oxygen molar flow rate per area is:

$$\dot{n}_{O_2} = \frac{\dot{N}_{O_2}}{A} \quad (16)$$

where  $A$  is the area of the membrane-electrode-assembly.

The water flow rate through the anode is the water consumed by the reaction as well as the water transported to the other side of the membrane:

$$\dot{N}_{H_2O,an} = \dot{N}_{H_2O,mem} + \dot{N}_{H_2O,cons} \quad (17)$$

$$\dot{N}_{H_2O,cons} = \frac{I}{2F} \quad (18)$$

The water molar flow rate per area at the anode is:

$$\dot{n}_{H_2O,an} = \frac{\dot{N}_{H_2O,an}}{A} \quad (19)$$

The molar flow rate of each species at the anode allows us to calculate the molar fraction of each species inside the anode:

$$y_{O_2,an} = \frac{\dot{n}_{O_2}}{\dot{n}_{O_2} + \dot{n}_{H_2O,an}} \quad (20)$$

$$y_{H_2O,an} = \frac{\dot{n}_{H_2O,an}}{\dot{n}_{O_2} + \dot{n}_{H_2O,an}} \quad (21)$$

With these molar fractions, the concentrations and partial pressure at the anode are:

$$C_{O_2,an} = \frac{P_{an} y_{O_2,an}}{RT_{an}} \quad (22)$$

Applying Fick's law, the concentration at the membrane-anode interface can be calculated:

$$C_{O_2,mem} = C_{O_2,an} + \frac{\delta_{e,an}}{D_{eff,an}} \dot{n}_{O_2} \quad (23)$$

where  $\delta_{e,an}$  is the anode thickness, and  $D_{eff,an}$  is the effective diffusion coefficient at the anode.

This diffusion coefficient is calculated in the membrane module.

The molar fractions are calculated at the membrane-anode interface:

$$y_{O_2,mem} = \frac{RT_{an}}{P_{an}} C_{O_2,mem} \quad (24)$$

Then the partial pressures can be calculated as:

$$P_{O_2,mem} = y_{O_2,mem} P_{an} \quad (25)$$

### 1.2.2 Cathode module

The half-cell reaction taking place at the cathode module is:



The hydrogen flow rate inside the cathode is calculated as:

$$\dot{N}_{H_2} = \dot{N}_{H_2,cat,in} - \dot{N}_{H_2,cat,out} + \dot{N}_{H_2,gen} \quad (27)$$

$$\dot{N}_{H_2,gen} = \frac{I}{2F} \quad (28)$$

The hydrogen molar flow rate per area is:

$$\dot{n}_H = \frac{\dot{N}_{H_2}}{A} \quad (29)$$

The water flow rate inside the cathode is the amount of water flowing from the anode through the membrane to the cathode:

$$\dot{N}_{H_2O,cat} = \dot{N}_{H_2O,mem} \quad (30)$$

The water molar flow rate per area at the cathode is:

$$\dot{n}_{H_2O,cat} = \frac{\dot{N}_{H_2O,cat}}{A} \quad (31)$$

Like the anode, the molar fractions of each species inside the cathode are:

$$y_{H_2,cat} = \frac{\dot{n}_{H_2}}{\dot{n}_{H_2} + \dot{n}_{H_2O,cat}} \quad (32)$$

$$y_{H_2O,an} = \frac{\dot{n}_{H_2O,cat}}{\dot{n}_H + \dot{n}_{H_2O,cat}} \quad (33)$$

which can then be used to calculate the concentration of each species inside the cathode:

$$C_{H_2,cat} = \frac{P_{cat} y_{H_2,cat}}{RT_{cat}} \quad (34)$$

where the molar fraction of each species inside the cathode is calculated using Fick's law:

$$C_{H_2,mem} = C_{H_2,cat} + \frac{\delta_{e,cat}}{D_{eff,cat}} \dot{n}_{H_2} \quad (35)$$

where  $\delta_{e,cat}$  is the cathode thickness, and  $D_{eff,cat}$  is the effective diffusion coefficient at the cathode. This diffusion coefficient is calculated in the membrane module.

The molar fractions at the membrane-anode interface can be calculated:

$$y_{H_2,mem} = \frac{RT_{cat}}{P_{cat}} C_{H_2,mem} \quad (36)$$

Then the partial pressures can be calculated as:

$$P_{H_2,mem} = y_{H_2,mem} P_{cat} \quad (37)$$

### 1.2.3 Membrane module

The membrane module describes the transport of water through the membrane. The water moves through the membrane through electro osmotic drag and diffusion. The electro osmotic drag happens as the  $H^+$  ions moving through the membrane and drags some water molecules with them.

The amount of water dragged through this phenomenon is described as:

$$\dot{N}_{H_2O,eod} = \frac{n_d I}{F} \quad (38)$$

where  $n_d$  is the electro-osmotic drag coefficient, in units of  $mol_{H_2O}/mol_{H^+}$ .

The diffusion of water due to the presence of water concentration gradient can be calculated as:

$$\dot{N}_{H_2O,diff} = D_w \left( \frac{C_{H_2O,mem,cat} - C_{H_2O,mem,an}}{t_{me}} \right) MW_{H_2O} A \quad (39)$$

where  $C_{H_2O,mem,cat}$  and  $C_{H_2O,mem,an}$  are the water concentration at the membrane on the cathode and anode side respectively.  $t_{me}$  is the thickness of the membrane,  $D_w$  is the diffusion coefficient of water, and A is the area. The water concentration at both sides of the membrane can be calculated as a function of the water concentration in the electrode channel. Using Fick's law of diffusion:

$$C_{H_2O,mem,cat} = C_{H_2O,cat} + \frac{\delta_{e,cat}}{D_{eff,cat}} \dot{n}_{H_2O,cat} \quad (40)$$

$$C_{H_2O,mem,an} = C_{H_2O,an} + \frac{\delta_{e,an}}{D_{eff,an}} \dot{n}_{H_2O,an} \quad (41)$$

where  $D_{eff,an}$  and  $D_{eff,cat}$  are, respectively, the  $O_2/H_2O$  and the  $H_2/H_2O$  effective binary diffusion coefficients. They can be calculated by using the porosity correction applied to the diffusion coefficients. The following correlation [7] is used:

$$D_{eff, A-B} = D_{A-B} \epsilon \left( \frac{\epsilon - \epsilon_p}{1 - \epsilon_p} \right)^\alpha \quad (42)$$

where  $\epsilon$  is the porosity of electrodes,  $\epsilon_p$  is the percolation threshold,  $\alpha$  is an empirical coefficient.

The values used to calculate these parameters are presented in Table 3 [8] [9] [10] [11].

**Table 4**

Values to calculate effective binary diffusion coefficients

| Coefficient  | Value |
|--------------|-------|
| $\epsilon$   | 0.3   |
| $\epsilon_p$ | 0.11  |
| $\alpha$     | 0.785 |

$D_{A-B}$  is the binary diffusion coefficient for species A and B, which can be calculated using Eq. (43) as follows:

$$PD_{A-B} = a \left( \frac{T}{\sqrt{T_{c,A} T_{c,B}}} \right)^b (P_{c,A} P_{c,B})^{\frac{1}{3}} (T_{c,A} T_{c,B})^{\frac{5}{12}} \left( \frac{1}{MW_A} + \frac{1}{MW_B} \right)^{\frac{1}{2}} \quad (43)$$

where P is pressure in atm, T is temperature in K. Also, a and b are dimensionless empirical coefficients, with values given in Table 4.

**Table 5**

Values for dimensionless coefficients for the calculations of binary coefficients for species A and B.

| Coefficients | Pairs of two nonpolar gases | Pairs of $H_2O$ and a nonpolar gas |
|--------------|-----------------------------|------------------------------------|
| a            | $2.745 \times 10^{-4}$      | $3.640 \times 10^{-4}$             |
| b            | 1.823                       | 2.334                              |

$T_c, P_c, MW$  are the critical temperature, pressure and molecular weight of species A and B with values for  $H_2, O_2$ , and  $H_2O$  in Table 5.

**Table 6**

Critical temperature, pressure and molecular weight for hydrogen, oxygen and water.

|             | $H_2$ | $O_2$ | $H_2O$ |
|-------------|-------|-------|--------|
| $P_c(atm)$  | 12.8  | 49.7  | 218.3  |
| $T_c(K)$    | 33.3  | 154.4 | 647.3  |
| $MW(g/mol)$ | 2     | 32    | 18     |

The concentration of water at the electrodes can be calculated as:

$$C_{H_2O,an} = \frac{\rho_{H_2O}(T_{an})}{MW_{mem,H_2O}} \quad (44)$$

$$C_{H_2O,cat} = \frac{\rho_{H_2O}(T_{cat})}{MW_{mem,H_2O}} \quad (45)$$

The net water flow through the membrane can now be calculated as:

$$\dot{N}_{H_2O,mem} = \dot{N}_{H_2O,eod} + \dot{N}_{H_2O,diff} \quad (46)$$

The water molar fraction and pressure inside the membrane for cathode and anode can be calculated using Eqs. (47)-(48) and (49)-(50), respectively:

$$y_{H_2O,mem,cat} = \frac{C_{H_2O,mem,cat}}{C_{H_2O,mem,cat} + C_{H_2,mem}} \quad (47)$$



$$P_{H_2O,mem,cat} = y_{H_2O,mem,cat} P_{cat} \quad (48)$$

$$y_{H_2O,mem,an} = \frac{C_{H_2O,mem,an}}{C_{H_2O,mem,an} + C_{O_2,mem}} \quad (49)$$

$$P_{H_2O,mem,an} = y_{H_2O,mem,an} P_{an} \quad (50)$$

#### 1.2.4 Voltage module

The real cell voltage in an electrolyzer is higher than the ideal open-circuit voltage, and can be expressed as:

$$Vol = E + \eta_{act} + \eta_{ohm} \quad (51)$$

where  $Vol$  is the real cell voltage,  $E$  is the ideal open circuit voltage,  $\eta_{act}$  is the activation overvoltage, and  $\eta_{ohm}$  is the Ohmic overvoltage. The calculations of each term are presented by Eqs. (52)-(56).

Open circuit voltage is calculated by using the Nernst equation:

$$E = E_{rev}^0 + \frac{RT}{2F} \left[ \ln \left( \frac{P_{H_2} P_{O_2}^{\frac{1}{2}}}{P_{H_2O}} \right) \right] \quad (52)$$

where  $E_{rev}^0$  is the reversible cell potential at standard temperature and pressure. It is modeled by an empirical temperature dependence equation:

$$E_{rev}^0 = 1.229 - 0.9 \times 10^{-3} (T - 298) \quad (53)$$

Activation overpotential is calculated as the sum of the activation overpotential on both the anode and the cathode side, as presented by Eqs. (54)-(56).

$$V_{act,an} = \frac{RT_{an}}{\alpha_{an} F} \operatorname{arcsinh} \left( \frac{i}{2i_{0,an}} \right) \quad (54)$$

$$V_{act,cat} = \frac{RT_{cat}}{\alpha_{cat} F} \operatorname{arcsinh} \left( \frac{i}{2i_{0,cat}} \right) \quad (55)$$

$$\eta_{act} = V_{act,an} + V_{act,cat} \quad (56)$$

where  $i_{0,an}$  and  $i_{0,cat}$  are the exchange current density at anode and cathode electrodes, respectively, and  $\alpha_{an}$  and  $\alpha_{cat}$  are the charge transfer coefficients at anode and cathode electrodes, respectively. The values for these parameters are given in Table 6.

**Table 7**

Parameters to calculate activation overpotential.

|          | Anode              | Cathode            |
|----------|--------------------|--------------------|
| $i_0$    | $2 \times 10^{-7}$ | $2 \times 10^{-3}$ |
| $\alpha$ | 2                  | 0.5                |

Ohmic overpotential can be calculated using Eqs. (57)-(59) as follows:

$$\eta_{ohm} = i R_{ohm} \quad (57)$$

$$R_{ohm} = \frac{t_{me}}{\sigma_{me}} \quad (58)$$

$$\sigma_{me} = (0.01539 \lambda - 0.00326) \exp \left[ 1268 \left( \frac{1}{303} - \frac{1}{T} \right) \right] \quad (59)$$

where  $t_{me}$  is the membrane thickness,  $\sigma_{me}$  is the material conductivity,  $i$  is the current density of the electrolyzer,  $T$  is the temperature of the electrolyzer, and  $\lambda$  is the membrane water content.

### 1.3 Salt Cavern Model

To pump hydrogen into the salt cavern, hydrogen is compressed to a pressure that is higher than the pressure of the salt cavern. The thermodynamic parameters of compressing this hydrogen are taken from [12]. The amount of power needed to compress the hydrogen produced is:

$$W_{comp} = \dot{N}_{H_2} [H_{H_2}(P_{comp,out}, T_{comp,out}) - H_{H_2}(P_{comp,in}, T_{comp,in})] \quad (60)$$

where  $H_{H_2}(P_{comp,out}, T_{comp,out})$  is the enthalpy of hydrogen at the outlet pressure and temperature of the compressor, and  $H_{H_2}(P_{comp,in}, T_{comp,in})$  is the enthalpy of hydrogen at the inlet pressure and temperature of the compressor.

The salt cavern has a minimum and maximum pressure threshold. These thresholds are needed to maintain geotechnical safety of the salt cavern. The lower bound pressure limit is to help maintain the capability for gas injection as well as gas withdrawal [13]. It also makes sure that the cavern salt cavern is stable and will not cave in [14]. The maximum pressure limit is to prevent the salt cavern from rock fracturing, resulting from the high pressure on the cavern wall [15]. The minimum and maximum cavern pressure can be calculated as follows:

$$P_{min} = 0.24(P_{overburden}) \quad (61)$$

$$P_{max} = 0.80(P_{overburden}) \quad (62)$$

$$P_{overburden} = \rho_{rock} g (D - H) \quad (63)$$

where  $P_{min}$  is the minimum pressure of the salt cavern,  $P_{max}$  is the maximum pressure of the salt cavern.  $P_{overburden}$  is the overburden pressure, or sometimes called lithostatic pressure.  $\rho_{rock}$  is the density of the rock in  $kg\ m^{-3}$ ,  $g$  is the gravitational acceleration (assumed as  $9.81\ m\ s^{-2}$ ),  $D$  is the cavern depth in m, and  $H$  is the cavern height in meters.

#### 1.4 Brayton Cycle Model

The compressor can be modeled as:

$$T_{comp,out} = T_{amb} \left( 1 + \frac{x_c - 1}{\eta_{comp}} \right) \quad (64)$$

$$x_c = \left( \frac{PR_c \dot{m}_a}{\dot{m}_{a,nom}} \right)^{\frac{\gamma_c - 1}{\gamma_c}} \quad (65)$$

where  $T_{comp,out}$  is the outlet temperature of the compressor,  $T_{amb}$  is the ambient temperature, which can be used as inlet temperature of the compressor,  $\eta_{comp}$  is the efficiency of the compressor,  $PR_c$  is the compressions ratio,  $\dot{m}_{a,nom}$  is the nominal intake air flow rate, and  $\gamma_c$  is the cold end ratio of specific heats. The air flow rate can be calculated using:

$$\dot{m}_a = \frac{P_{amb}}{P_{amb,o}} \sqrt{\frac{T_{amb,o}}{T_{amb}}} \frac{\sin(\theta_{IGV} - \theta_{min})}{\sin(\theta_{max} - \theta_{min})} \dot{m}_{a,nom} \quad (66)$$

where  $P_{amb}$  is the ambient pressure,  $P_{amb,o}$  is the ambient reference pressure,  $T_{amb,o}$  is the ambient reference temperature,  $\theta_{IGV}$  is the angle of the IGVs,  $\theta_{min}$  and  $\theta_{max}$  are the minimum and maximum IGV angles respectively.

For the combustion chamber model, the turbine firing temperature, which is the exit temperature of the combustion chamber, can be modeled using Eq. (67) as follows:

$$T_{fire} = T_{comp,in} + \left( \frac{\eta_{comb} LHV}{C_{p,e}} \right) \left( \frac{\dot{m}_f}{\dot{m}_f + \dot{m}_a} \right) \quad (67)$$

where  $T_{comp,in}$  is the temperature going into the compressor,  $\dot{m}_f$  is the fuel (hydrogen) flow rate,  $\eta_{comb}$  is the combustion efficiency, LHV is the lower heating value of hydrogen, and  $C_{p,e}$  is the specific heat of the exhaust gas flow.

The turbine exhaust temperature can be modeled by relating it to the firing temperature in the following equation:

$$T_e = T_{fire} \left( 1 - \left( 1 - \frac{1}{x_h} \right) \eta_{turb} \right) \quad (68)$$

$$x_h = \left( PR_T \frac{\dot{m}_f + \dot{m}_a}{\dot{m}_{f,nom} + \dot{m}_{a,nom}} \right)^{\frac{\gamma_h - 1}{\gamma_h}} \quad (69)$$

$T_e$  is the turbine exhaust temperature,  $\eta_{turb}$  is the turbine efficiency,  $\dot{m}_{f,nom}$  is the nominal fuel flow, and  $\gamma_h$  is the hot end ratio of the specific heats. From these temperatures, the steady state power generation of the plant can be calculated:

$$W_{GasTurb} = (\dot{m}_f + \dot{m}_a) C_{p,e} (T_{fire} - T_e) - \dot{m}_a C_{p,a} (T_{comp,out} - T_{amb}) \quad (70)$$

where  $C_{p,a}$  is the heat capacity of air, which is assumed to be constant for this model.

The recuperation is modeled as follows:

$$T_{comp,in} = \eta_{recup}(T_e - T_{comp,out}) + T_{comp,out} \quad (71)$$

$$T_{recup} = \frac{T_e - \dot{m}_a C_{p,a}(T_{c,in} - T_d)}{(\dot{m}_f + \dot{m}_a)C_{p,e}} \quad (72)$$

where  $\eta_{recup}$  is the efficiency of the recuperator, assumed at 75%.  $T_{recup}$  is the outlet temperature of the recuperator.

## 4.5 Model Validation

This section presents the validation results for different subsystems of the hybrid energy system. Note that for the steam Rankine cycle, the model has been validated previously in [16] and the validation results are not presented here.

### 1.5.1 NuScale power plant

To validate the developed model for the nuclear core, the results of this study are compared against those presented in the study of Gabor et al. [1] using the following input parameters presented in Table 7:

**Table 7**

Input parameter used for nuclear core model.

| Parameter (unit)               | Value                    |
|--------------------------------|--------------------------|
| $\alpha_f (\$/^\circ\text{C})$ | $-5.326 \times 10^{-3}$  |
| $\alpha_m (\$/^\circ\text{C})$ | $-2.018 \times 10^{-2}$  |
| $\phi_0 (cm^{-2}s^{-1})$       | $1.3018 \times 10^{13}$  |
| $\sigma_x (cm^2)$              | $2.8041 \times 10^{-18}$ |

Table 8 shows the validation results in terms of neutron flux (%) and moderator temperature for different control rods positions. As can be seen, the results of this study show a very good agreement with those of Gabor et al. [1].

**Table 8**

Validation results for the reactor core.

| Control Rods<br>Position (m) | Neutron Flux (%) |                  | Moderator Temperature ( $^{\circ}\text{C}$ ) |                  |
|------------------------------|------------------|------------------|----------------------------------------------|------------------|
|                              | This study       | Gabor et al. [1] | This study                                   | Gabor et al. [1] |
| 0                            | 100              | 100              | 280.2                                        | 280.2            |
| 0.18                         | 97.5             | 96.1             | 279.3                                        | 278.5            |
| 0.25                         | 94.0             | 93.1             | 278.5                                        | 278              |

### 1.5.2 Electrolyzer

The voltage and efficiency of the electrolyzer are used as an indicator to validate the accuracy of the developed electrolyzer model. For these validations, the following input parameters presented in Table 9 are used.

**Table 9**

Input parameters for hydrogen electrolyzer.

| Parameter (unit)           | Value                   |
|----------------------------|-------------------------|
| Anode temperature (K)      | 298.15                  |
| Anode pressure (Pa)        | 101325                  |
| Anode thickness (m)        | $8 \times 10^{-5}$      |
| Cathode temperature (K)    | 298.15                  |
| Cathode pressure (Pa)      | 101325                  |
| Cathode thickness (m)      | $8 \times 10^{-5}$      |
| Membrane thickness (m)     | $0.1756 \times 10^{-5}$ |
| Area ( $\text{m}^2$ )      | $160 \times 10^{-4}$    |
| $D_w(\text{m}^2/\text{s})$ | $1.28 \times 10^{-10}$  |

In terms of voltage, and the results are compared against those presented by [17]. The voltage validation results are presented in Figure 1, showing the variation of voltage with current density. According to Figure 1, the results of this study have a close agreement with those of [17]. The average percentage error between the results of this study and the results of [17] is 1.67%.

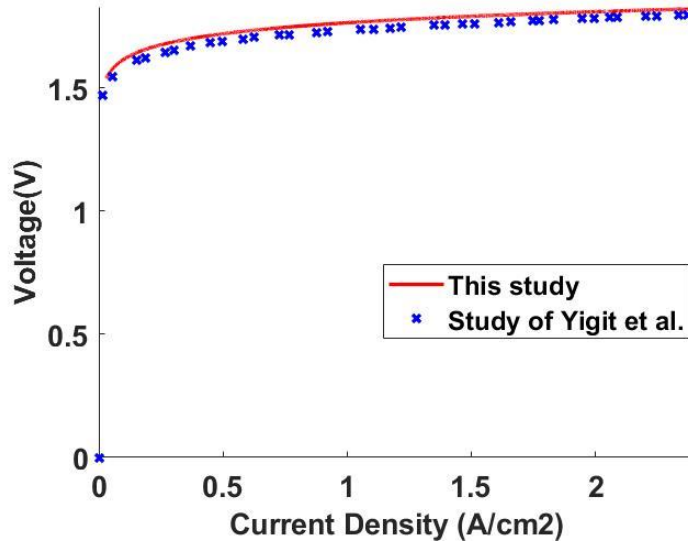


**Figure 1.** Comparison between the voltage of the proposed model and Yigit et al.'s model [17].

To further validate the model, the efficiency of the electrolyzer is compared with the results found in [17] for different values of current densities and the validation results are presented in Figure 4. It is found that the results of this study are in excellent agreement with those of [17], with an average percentage error of 1.1%.

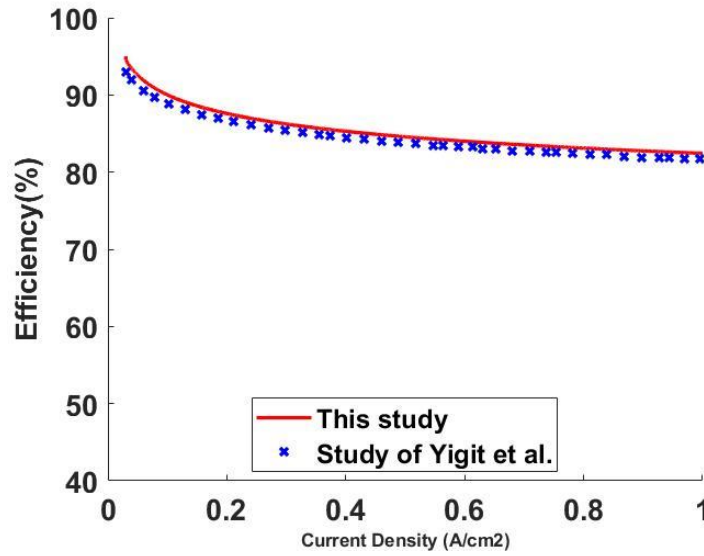


**Figure 3.** Comparison between the efficiency of the proposed model and Yigit et al's model [17].

### 1.5.3 Salt Cavern

The results of the developed salt cavern model are compared with the results taken from [18] for the following input parameters given in Table 10. Figure 5 shows the validation results in terms of variation of hydrogen pressure with time. As noticed, the results of this study have an excellent agreement with those presented in [18].

**Table 10**

Input used to validate the developed salt cavern model.

| Input parameter                          | This study            |
|------------------------------------------|-----------------------|
| Initial Pressure (MPa)                   | 2                     |
| Initial Temperature (K)                  | 290                   |
| Hydrogen compressibility                 | A function of T and P |
| Hydrogen dynamic viscosity (Pa·s)        | A function of T and P |
| Volume ( $m^3$ )                         | 40,000                |
| Injected/extracted mass flow rate (kg/s) | 0.034                 |



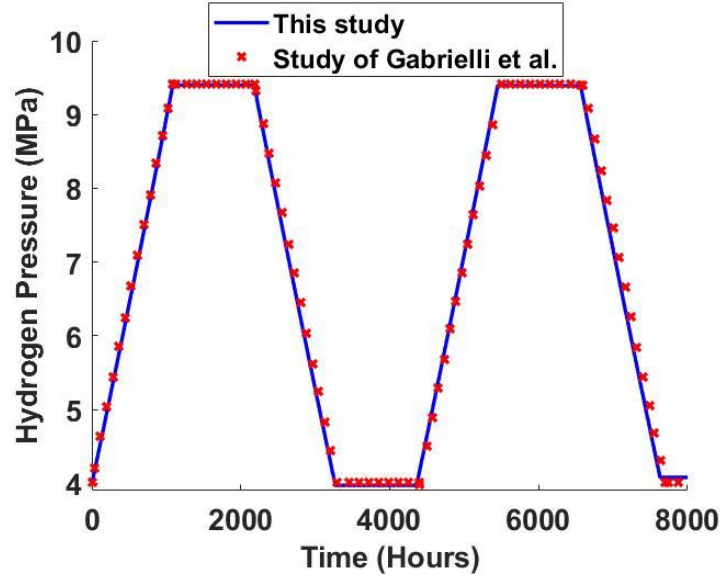


**Figure 4.** Comparison between the proposed model and Gabrielli et al.'s model [18].

#### 1.5.4 Gas Turbine

Using natural gas as a fuel, the gas turbine cycle model was previously validated in [16]. Since there is no available gas turbine that uses just purely hydrogen as fuel, some assumptions are made in the proposed model. To validate the results using in this model, the hydrogen gas turbine efficiency is compared with the reported efficiency of a mixed natural gas/hydrogen fuel gas turbine efficiency made by Mitsubishi. The recorded efficiency of the Mitsubishi turbine is 63% [19]. The calculated efficiency of the proposed gas turbine cycle (Brayton cycle) when run with a fuel flow of 0.2 kg/s is 55.37%, which is comparable. The reason for a lower performance is that a simple recuperative cycle is used, which is not optimized for the gas turbine. In future work, the system will be optimized to the flow rate and temperature of the gas turbine. The objective of the paper is not to propose a new hydrogen gas turbine, but the overall integration feasibility study of the NHES.

## **2. Supplemental Results and Discussion**

## 2.1 Comparison results for April and May

To compare the results of the NHES and a stand-alone reactor, Figures 1 and 2 present the simulation result of a stand-alone nuclear reactor for April and May. Figures 1 and 2 (a) show the total demand of the grid as well as the power produced by the stand-alone reactor for April and May, respectively. Figure 1 and 2 (b) show the positions of the control rods ramping up and down to regulate the amount of power produced by the nuclear reactor for April and May, respectively.

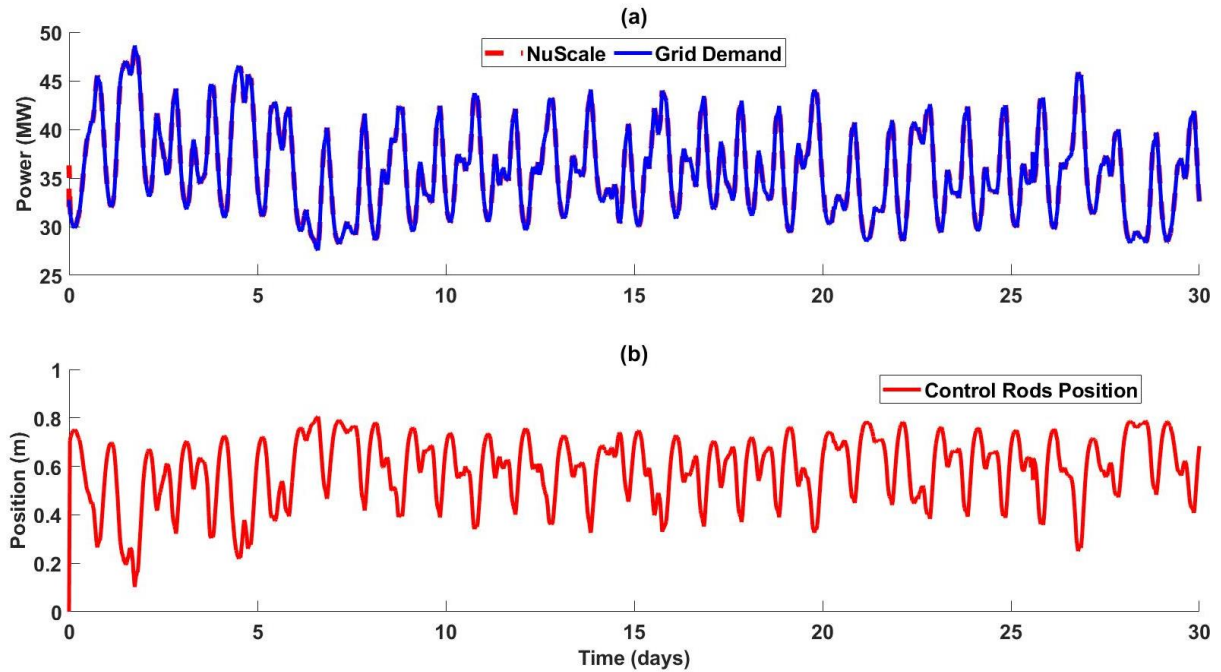


**Figure 1.** Stand-alone nuclear reactor simulation results for April 2020: (a) power output of the stand-alone NuScale plant, and (b) control rods position of the stand-alone NuScale plant.

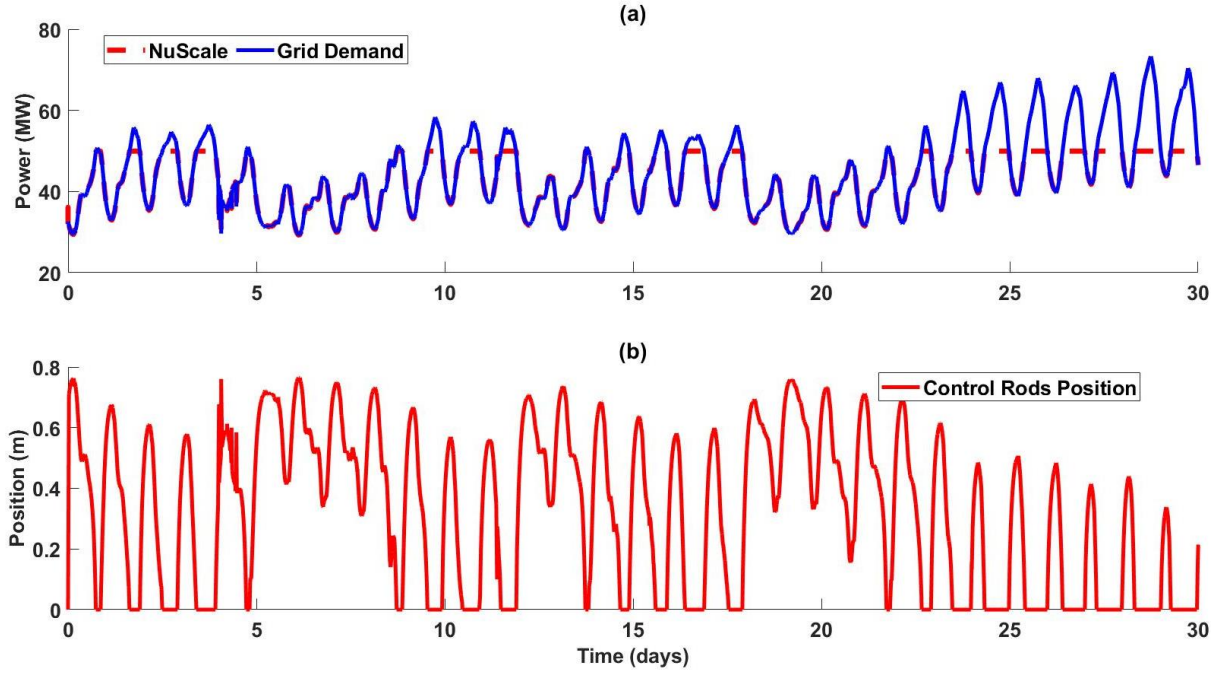


**Figure 25.** Stand-alone nuclear reactor simulation results for May 2020: (a) power output of the stand-alone NuScale plant, and (b) control rods position of the stand-alone NuScale plant.

As shown by Figures 1 and 2 (a), the grid demand (shown in blue lines) fluctuates from 27.5 MW to 73.3 MW across April and May. There are 19 periods covering 15.6% of the months in which the grid demand rises above the nominal capacity of the NuScale plant. In these cases, the plant cannot meet the demand of the grid, and additional power from other electricity sources should be purchased. Therefore, for the month of April and May, the stand-alone NuScale plant can only meet the demand 84.4% of the time. According to Figures 1 and 2 (a) and Figures 1 and 2 (b), when the demand is lower than the nominal capacity of the NuScale plant, the plant is forced to ramp down to not overload the grid with excess electricity leading to a change in the control rods position. In the month of April and May, to follow the grid demand, there are 89 ramping cycles compared to 39 for the NHES. In April and May, the stand-alone reactor produces 57.7 MWh compared to 67.1 MWh produced by the NHES.

## References

- [1] A. Gabor, C. Fazeska and K. M. Hangos, "Modeling and Identification of a Nuclear Reactor with Temperature Effects and Xenon poisoning," in *IEEE Xplore*, 2009.
- [2] M. Johnson, S. Lucas and P. Tsvetkov, "Modeling of Reactor Kinetics and Dynamics," INL, Idaho Falls, 2010.
- [3] K. Frick, "Status Report on the NuScale Module Developed in the Modelica Framework," Idaho National Lab, 2019.
- [4] A. Sadegh-Noedoost, F. Faghihi, A. Fakhraei and M. Amin-Mozafari, "Investigations of the fresh-core cycle-length and the average fuel depletion analysis of the NuScale core," *Annals of Nuclear Energy*, vol. 136, February 2020.
- [5] D. L. Hetrick, *Dynamics of Nuclear Reactors*, USA: American Nuclear Society, 1993.
- [6] F. D'Auria, *Thermal-Hydraulics of Water Cooled Nuclear Reactors*, Woodhead Publishing, 2017.
- [7] M. M. Tomadakis and S. V. Sotirchos, "Ordinary and transition regime diffusion in random fiber structures," *AIChE Journal*, 1993.
- [8] M. Santarelli, "idrogeno e celle a combustibile".
- [9] M. G. L. Santarelli, M. F. Torchio and P. Cochis, "Parameters estimation of a PEM fuel cell polarization curve and analysis of their behavior with temperature," *Journal of Power Sources*, pp. 824-835, 2006.
- [10] J. C. Amphlett, R. M. Baumert, R. F. Mann, B. A. Peppley, P. R. Roberge and T. J. Harris,, "Performance modelling of the ballard mark iv solid polymer electrolyte fuel cell," *Journal of The Electrochemical Society*, vol. 142, 1995.
- [11] J. H. Nam and M. Kaviany, "Effective diffusivity and water-saturation distribution in single- and two-layer PEMFC diffusion medium," *International Journal of Heat and Mass Transfer*, vol. 46, no. 24, pp. 4595-4611, 2003.
- [12] A. Witkowski, A. Rusin, M. Majkut and K. Stolecka, "Comprehensive analysis of hydrogen compression and pipeline transportation from thermodynamics and safety aspects," *Energy*, vol. 141, pp. 2508-2518, 15 December 2017.
- [13] D. G. Caglayan, N. Weber, H. Heinrichs, J. Linßen, M. Robinius, P. A. Kukla and D. Stolten, "Technical Potential of Salt Caverns for Hydrogen Storage in Europe," *International Journal of Hydrogen Energy*, 2020.
- [14] Y. Wang, J. Kowal, M. Leuthold and D. U. Sauer, ""Storage System of Renewable Energy Generated Hydrogen for Chemical Industry," *Energy Procedia*, pp. 657-667, 2012.

- [15] HyUnder, "Assessment of the potential, the actors and relevant business cases for large scale and seasonal storage of renewable electricity by hydrogen underground storage in Europe," 2014.
- [16] K. Ellingwood, K. Mohammadi and K. Powell, "A novel means to flexibly operate a hybrid concentrated solar power plant and improve operation during non-ideal direct normal irradiation conditions," *Energy Conversion and Management*, 2020.
- [17] T. Yigit and O. F. Selamet, "Mathematical modeling and dynamic Simulink simulation of high-pressure PEM electrolyzer system," *International Journal of Hydrogen Energy*, pp. 13901-13914, 2016.
- [18] P. Gabrielli, A. Poluzzi, G. J. Kramer, C. Spiers, M. Mazzotti and M. Gazzani, "Seasonal energy storage for zero-emissions multi-energy systems via underground hydrogen storage," *Renewable and Sustainable Energy Reviews*, vol. 121, 2020.
- [19] Mitsubishi Power, "MHPS Successfully Tests Large-scale High-efficiency Gas Turbine Fueled by 30% Hydrogen Mix -- Will Contribute to Reducing CO2 Emissions during Power Generation --," *Mitsubishi Power*, 19 Jan 2018.